



UNIVERSITÀ DI PISA

Department of Physics Masters Degree in Physics

Characterization of monolithic CMOS pixel sensors for charged particle detectors and for high intensity dosimetry

6 Candidate:
Ravera Eleonora

Supervisor:
Francesco Forti

7 Academic year 2021/2022

⁸ Contents

⁹	1 Characterization	4
¹⁰	1.1 TJ-Monopix1 characterization	4
¹¹	1.1.1 Threshold and noise: figure of merit for pixel detectors	4
¹²	1.1.2 Linearity of the ToT	8
¹³	1.1.3 Calibration of the ToT	9
¹⁴	1.1.4 Changing the bias	14
¹⁵	1.1.5 Measurements with radioactive sources	15
¹⁶	1.1.6 Dead time measurements	20
¹⁷	1.2 ARCADIA-MD1 characterization	22
¹⁸	2 Test beam measurements	26
¹⁹	2.1 Apparatus description	27
²⁰	2.1.1 Accelerator	27
²¹	2.1.2 Mechanical carriers	27
²²	2.2 Measurements	28
²³	Bibliography	33

²⁴ **Chapter 1**

²⁵ **Characterization**

²⁶ Rifai il conto della lunghezza di attenuazione. Ho trovato (presentazione Luciano Mus) 29
²⁷ um per ka e 37 um per kb.

²⁸ **1.1 TJ-Monopix1 characterization**

²⁹ **1.1.1 Threshold and noise: figure of merit for pixel detectors**

³⁰ A characterization of threshold and noise is typically necessary since these values have an
³¹ impact on the operating conditions and on the performance of the chips, so much that
³² the signal to threshold ratio may be considered as the figure of merit for pixel detectors
³³ rather than the signal to noise ratio. The mean minimum stable threshold evolved through
³⁴ different generation of chips: in the 1st generation it was around 2500 e^- while in the 3rd
³⁵ (corresponding to nowadays chips) is less than 500 e^- . This allows in thinner sensors with
³⁶ smaller signals: from $16\,000 \text{ e}^-$ produced in $200 \mu\text{m}$, the signal expected moved down to
³⁷ 2000 e^- produced in $25 \mu\text{m}$. In agreement with this, the threshold of TJ-Monopix1 is
³⁸ around 500 e^- .

³⁹ Obviously the threshold has to be located between the noise peak around the baseline
⁴⁰ and the signal distribution, in particular it has to be low enough to maintain a high signal
⁴¹ efficiency, but also high enough to cut the noise: for a low threshold many pixels can fire
⁴² at the same time and a positive feedback can set off a chain reaction eventually, causing
⁴³ all the other pixels to fire. Thus, the noise sets a lower bound to the threshold: if an
⁴⁴ occupancy $\leq 10^{-4}$ is required, for example, a probability of firing lower than that value
⁴⁵ is needed and this, assuming a gaussian noise, requires that the threshold is set at least
⁴⁶ 3.7σ , with σ the RMS of the noise. In this case, if the noise is 100 e^- (reasonable), the
⁴⁷ threshold must be higher than $3.7 \times 100 \text{ e}^-$. Typically this argument sets only a minimal
⁴⁸ bound to the threshold since the variation with time and from pixel to pixel have to be
⁴⁹ taken into account: the temperature, the annealing (for example, the radiation damages in
⁵⁰ the oxide layer causes shift of MOSFET threshold voltage) and the process parameters
⁵¹ variation across the wafer (as for example process mismatch between transistors).

⁵² On the other hand, concerning the noise, given that the first stage of amplification is
⁵³ the most crucial, since in the following stages the signal amplitude is high compared to
⁵⁴ additional noise, it is valued at the preamplifier input node. Then, the noise is parame-
⁵⁵ terized as Equivalent Noise Charge (ENC), which is defined as the ratio between the noise
⁵⁶ N at the output expressed in Volt and the out voltage signal S produced by 1 e^- entering

57 in the preamplifier:

$$ENC = \frac{N_{out}[V]}{S_{out}[V/e-]} = \frac{V_{noise}^{RMS}}{G} \quad (1.1)$$

58 with G expressed in V/e-; as the gain increases, the noise reduces .

59 Considering the threshold dispersion a requirement for the ENC is:

$$ENC < \sqrt{(T/3.7)^2 - T_{RMS}^2(x) - T_{RMS}^2(t)} \quad (1.2)$$

60 where the T is the threshold set, T_{RMS} is the threshold variation during time (t) and
61 across the matrix (x); a typical reasonable value often chosen is 5 ENC.

62 Because of the changing of the 'real' threshold, the possibility of changing and adapting
63 the setting parameters of the FE, both in time and in space is desiderable: these parameters
64 are usually set by Digital to Analog Converter (DAC) with a number of bit in a typical
65 range of 3-7. Unfortunately DAC elements require a lot of space that may be not enough
66 on the pixel area; therefore, the FE parameters are typically global, which means that they
67 are assigned for the whole chip, or they can be assigned for regions the matrix is divided
68 into. The former case corresponds to TJ-Monopix1's design in which 7 bits are used for
69 a total 127-DAC possible values, while the latter corresponds to the ARCADIA-MD1's
70 one, **where quanti bit??**. An other possibility, for example implemented in TJ-Monopix2,
71 is allocate the space on each pixel for a subset of bits, then combinig the global threshold
72 with a fine tuning. If so, the threshold dispersion after tuning is expected to decrease
73 depening on the number of bits available for tuning:

$$\sigma_{THR,tuned} = \frac{\sigma_{THR}}{2^{nbit}} \quad (1.3)$$

74 where σ_{thr} is the RMS of the threshold spread before tuning.

75 To measure the threshold and noise of pixels a possible way is to make a scan with
76 different known injected charge: the threshold corresponds to the value where the efficiency
77 of the signal exceeds the 50%, and the ENC is determined from the slope at this point.
78 Assuming a gaussian noise, e.g. a noise whose transfer function turns a voltage δ pulse in a
79 gaussian distribution, the efficiency of detecting the signal and the noise can be described
80 with the function below:

$$f(x, \mu, \sigma) = \frac{1}{2} \left(1 + erf \left(\frac{x - \mu}{\sigma\sqrt{2}} \right) \right) \quad (1.4)$$

81 where erf is the error function. Referring to 1.4 the threshold and the ENC corresponds
82 to the μ and σ .

83 I used the injection circuit available on the chip to inject 100 pulses for each input
84 charge for a fixed threshold. The injection happens on a capacity at the input of the FE
85 circuit, whose nominal value is 230 aF and from which the conversion factor from DAC
86 units to electrons can be obtained: for the PMOS flavor, for example, since the DAC are
87 biased at 1.8 V, the Least significant Bit (LSB) corresponds to a voltage of 14.7 mV from
88 which the charge for LSB $1.43 \text{ e-}/\text{mV}$ and the conversion factor therefore is $20.3 \text{ e-}/\text{DAC}$.
89 While this value is equivalent for all the PMOS flavor, the HV flavor is expected to have a
90 different conversion factor, $\sim 33 \text{ e-}/\text{DAC}$, beacuse of the different input capacity. Besides
91 the charge, also the duration and the period of the injection pulse can be set; it is important
92 to make the duration short enough to have the falling edge during the dead time of the
93 pixel (in particular during the FREEZE signal) in order to avoid the undershoot, coming

	PMOS A	PMOS B	PMOS C	HV
Threshold [e ⁻]	401.70±0.15	400.78±0.24	539.66±0.58	403.87±0.19
Threshold dispersion [e ⁻]	32.90±0.11	32.97±0.17	55.54±0.42	44.67±0.15
Noise [e ⁻]	13.006±0.064	12.258±0.068	13.88±0.11	11.68±0.10
Noise dispersion [e ⁻]	1.608±0.044	1.504±0.046	1.906±0.072	1.580±0.068

Table 1.1: Mean threshold and noise parameters for all flavor and their dispersion on the matrix.

94 at high input charge, triggering the readout and reading spurious hits. Since the injection
 95 circuit is coupled in AC to the FE, if the falling edge of the pulse is sharp enough to
 96 produce an undershoot, this can be seen as a signal.

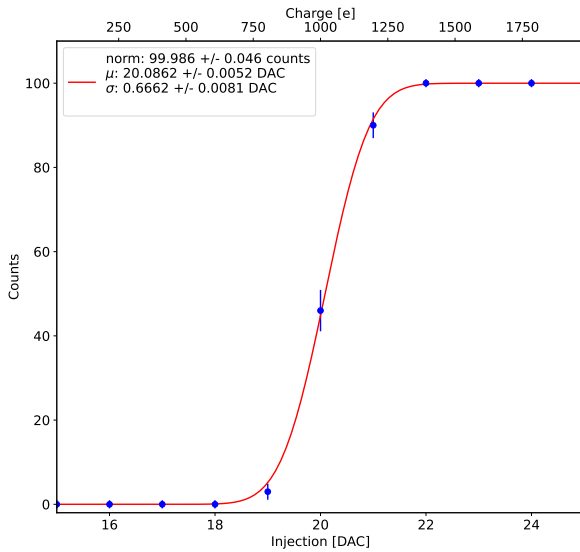


Figure 1.1: S-curve for pixel (10, 10) of the PMOS flavor (flavor B) with IDB fixed at 40 DAC. The conversion of charge injected from DAC to electrons has been performed using a nominal conversion factor of 20.3 e⁻/DAC *Mi sono resa conto che l'asse superiore è sbagliato. Devo rigenerare il plot*

97 with IDB equal to 40 DAC

98 Therefore I fitted the counts detected using the function in equation 1.4. Figure 1.1
 99 shows an example of such fit for a pixel belonging to the flavor B, while in figure 1.2 are
 100 shown the 1D and 2D distributions of the parameters found. I fitted the 1D distributions
 101 with a gaussian function to found the average and RMS of the noise and the threshold for
 102 each flavor across the matrix. The results are reported in table 1.1.

103 In the map at the top right panel of figure 1.2 (IDB=40 DAC) a slightly lower thresh-
 104 old is visible in the first biasing section (columns from 0 to 14); similar structures, but
 105 extended to the entire matrix, appear more evidently when using different IDB values.
 106 The systematic threshold variation across the biasing group has not a known motivation,
 107 but one could certainly be the transistor mismatch of the biasing DAC registers IDB
 108 and ICASN, which both adjust the effective threshold (I recall that ICASN regulate the

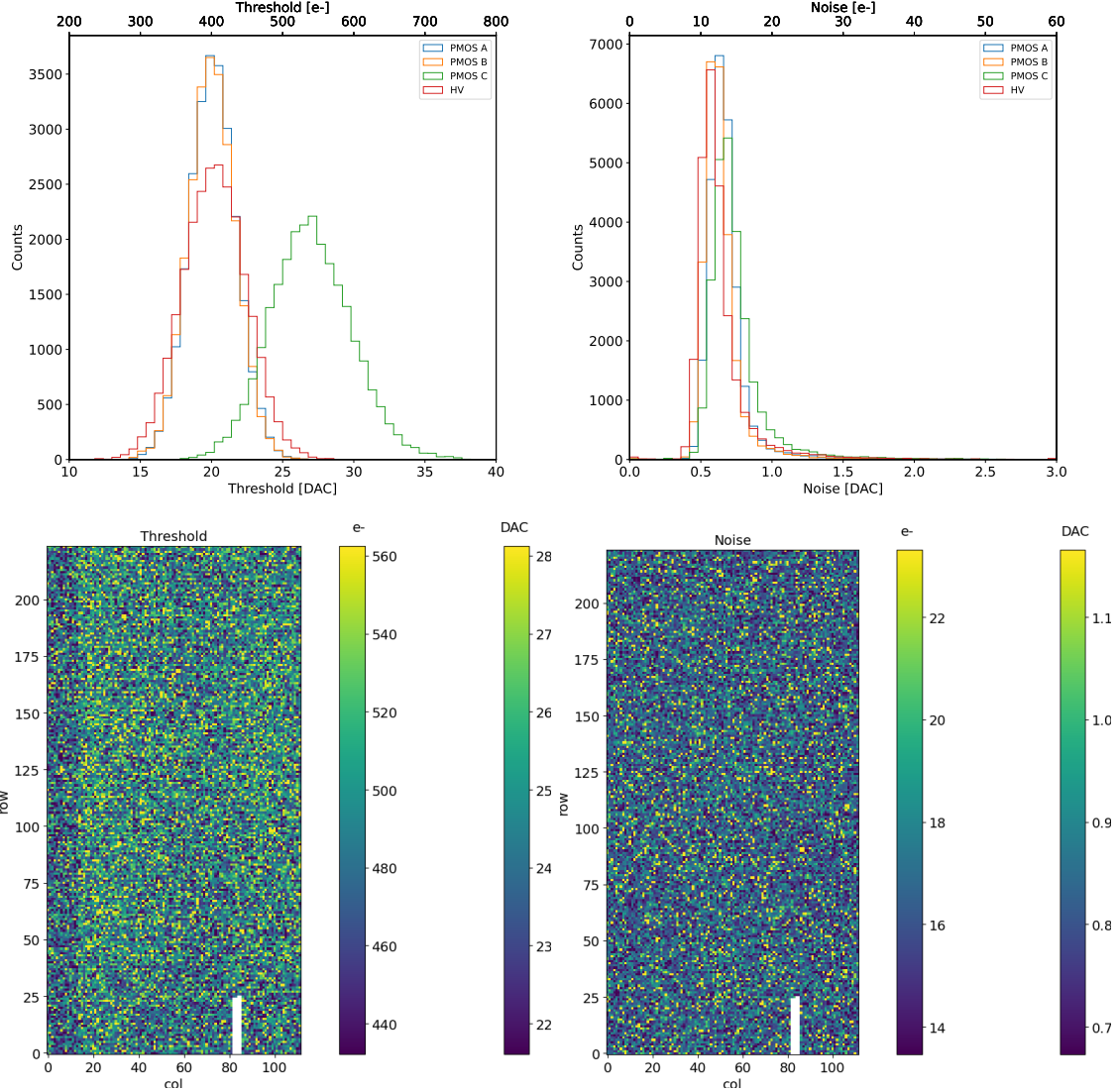


Figure 1.2: Histograms of the threshold (a) and the noise (b) found fitting the s-curve of all flavor with IDB fixed at 40 DAC. Below there are the maps of the threshold (a) and the noise (b), respectively, found fitting the s-curve with IDB fixed at 40 DAC for the PMOS flavor (B). The white pixels have the injection circuit broken.

109 baseline).

110 To verified the trend of the threshold as a function of the front end parameter IDB and
 111 find its dynamic range, I have permormed different scans changing the FE register IDB.
 112 For each IDB I have injected the whole matrix and search for the mean and the standard
 113 deviation of the threshold and noise distributions. The results are shown in figure 1.3:
 114 the blue points are the mean threhsold found whithin the matrix, while in green is shown
 115 the width of the threshold distribution, aka the threshold dispersion. While the threshold
 116 increases, the ENC decreases of $\sim 4 \text{ e-}$,which is $\sim 1/3$ of the noise at IDB=40 DAC.

117 Then, to evaluet the operation and the occupancy of the chip at different threshold
 118 I have made long acquisitions of noise at different IDB and check how the number of
 119 pixel masked changes with the threshold. The masking algorithm I have used search for
 120 pixels with rate $> 10 \text{ Hz}$ and mask them. With such algorithm, in our standard condition,

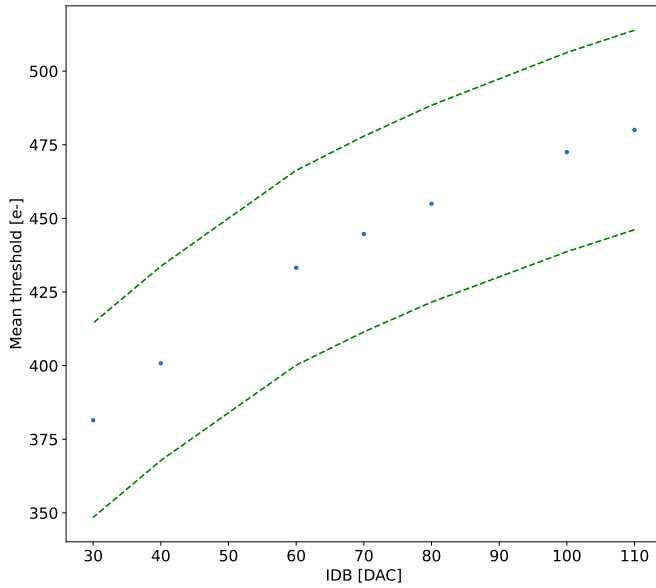


Figure 1.3: Flavor PMOS (B) with Psub-Pwell biased at -6 V. Threshold measured in electrons vs the register which sets the threshold, IDB.

121 IDB=40 DAC, a very low noise hit rate is intentionally achieved masking a dozen of pixels
 122 of the whole flavor.

123 1.1.2 Linearity of the ToT

124 I have already said in chapter ?? that TJ-Monopix1 returns an output signal proportional
 125 to the charge released by a particle in the epitaxial layer, which is the Time over Threshold;
 126 the ToT is saved as a 6-bit variable and then has a dynamic range equal to 0-64, which
 127 corresponds to 0 μ s to 1.6 μ s assuming a clock frequency of 40 MHz. When a pulse is longer
 128 than 1.6 μ s the counter rolls back to zero and there is no way to distinguish that charge
 129 from a lower one with the same ToT: that is the rollover of the ToT (1.4(a)).

130 In order to associate the ToT (in range 0-64) to the charge, a calibration of the signal
 131 is necessary. Assuming the linearity between ToT and the charge, Q can be found:

$$Q [DAC] = \frac{(ToT [au] - offset [au])}{slope [au/DAC]} \quad (1.5)$$

132 where m and q are the fitted parameters of the calibration. It is important to keep in mind
 133 that the main application target of TJ-Monopix1 is in the inner tracker detector of HEP
 134 experiments, then the main feature is the efficiency, then a rough calibration of the signal
 135 to charge is fine. The ToT information can be used both to better reconstruct the charge
 136 deposition in cluster in order to improve the track resolution, and for particle identification,
 137 especially for low momentum particles which do not reach the proper detectors.

138 The study of the output signal is made possible via the injection: since the pulses
 139 are triangular, the ToT is expected to be almost therefore, to prevent th linear. To verify
 140 this statement and study the deviations from linearity I fitted the ToT versus the charge
 141 injected for all the pixels within the matrix. In figure 1.4(b) there is an example of fit

for a pixel belonging to the flavor B, while in figure 1.5 there are the histograms and the maps of the parameters of the line-fit for all flavors with IDB fixed at 40 DAC. Here again a difference among the biasing section appears: since the slope of the ToT is related with the gain of the preamplifier (increasing the gain also increases the ToT), the mismatch is probably due to the transistor contributing to the amplification stage.

I fitted the average ToT of all the pulses recorded as a function of the pulse amplitude; data affected by rollover have been removed in order to avoid introducing a bias in the mean values. In figure 1.4 (b) are shown both the fits with a line (red) and with a second order polynomial (green): at the bounds of the ToT range values deviate from the line model. Since the deviation is lower than 1% and it only interests the region near the 0 and the 64, in first approximation it is negligible.

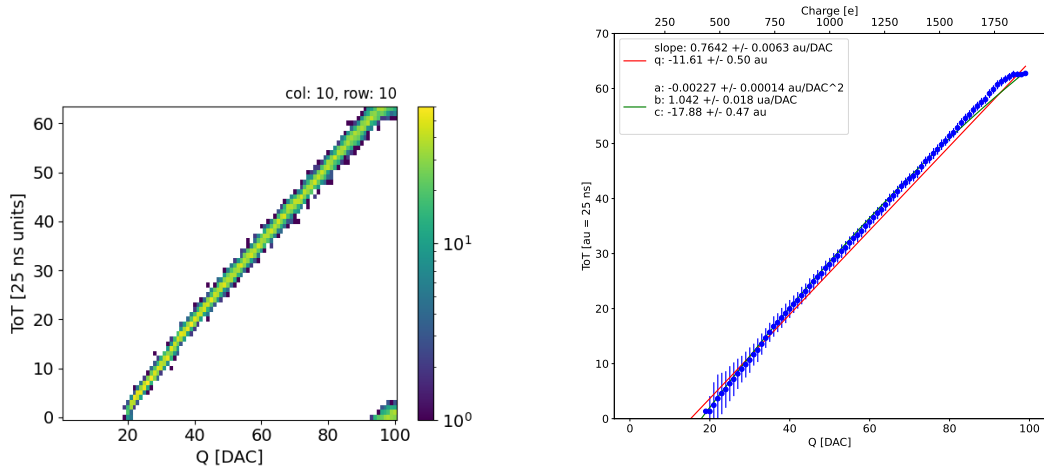


Figure 1.4: The figures refer to pixel (10,10) of the PMOS-reset flavor B with IDB fixed at 40 DAC. (a) Histogram of the injection pulses: the ToT is in range 0-64 since it is represented by 6 bit, so when achieving the 64 it rolls over back to the zero. (b) Mean ToT vs the the charge: the mean has been calculated cutted the rolling hits.

1.1.3 Calibration of the ToT

Finding a calibration for the ToT means defining a way to pass from the ToT values (0-64 clock counts) to a spectrum expressed in electrons collected. The principles of the calibration are the following: the ToT in clock counts maps (eq.1.1.2) a DAC range between the threshold and a value which depends on the pixel and generally is around 90-100 DAC. Assuming that a 0 DAC signal corresponds to 0 e⁻, if another reference point is fixed, a linear calibration function can be defined. After the calibration the ToT goes to map a charge range between the threshold and Q_{max} which is a function of the pixel and is around 2 ke⁻.

Moreover, considering that the charge injected in the FE goes to fill a capacitor C which is different from pixel to pixel, the true charge injected does not correspond to what expected assuming C equal to 230 aF, which is the nominal value. Accordingly to that, a measurement of this value provides both an absolute calibration of C and a conversion factor K to have a correspondence of the DAC signal in electrons. K and C are defined

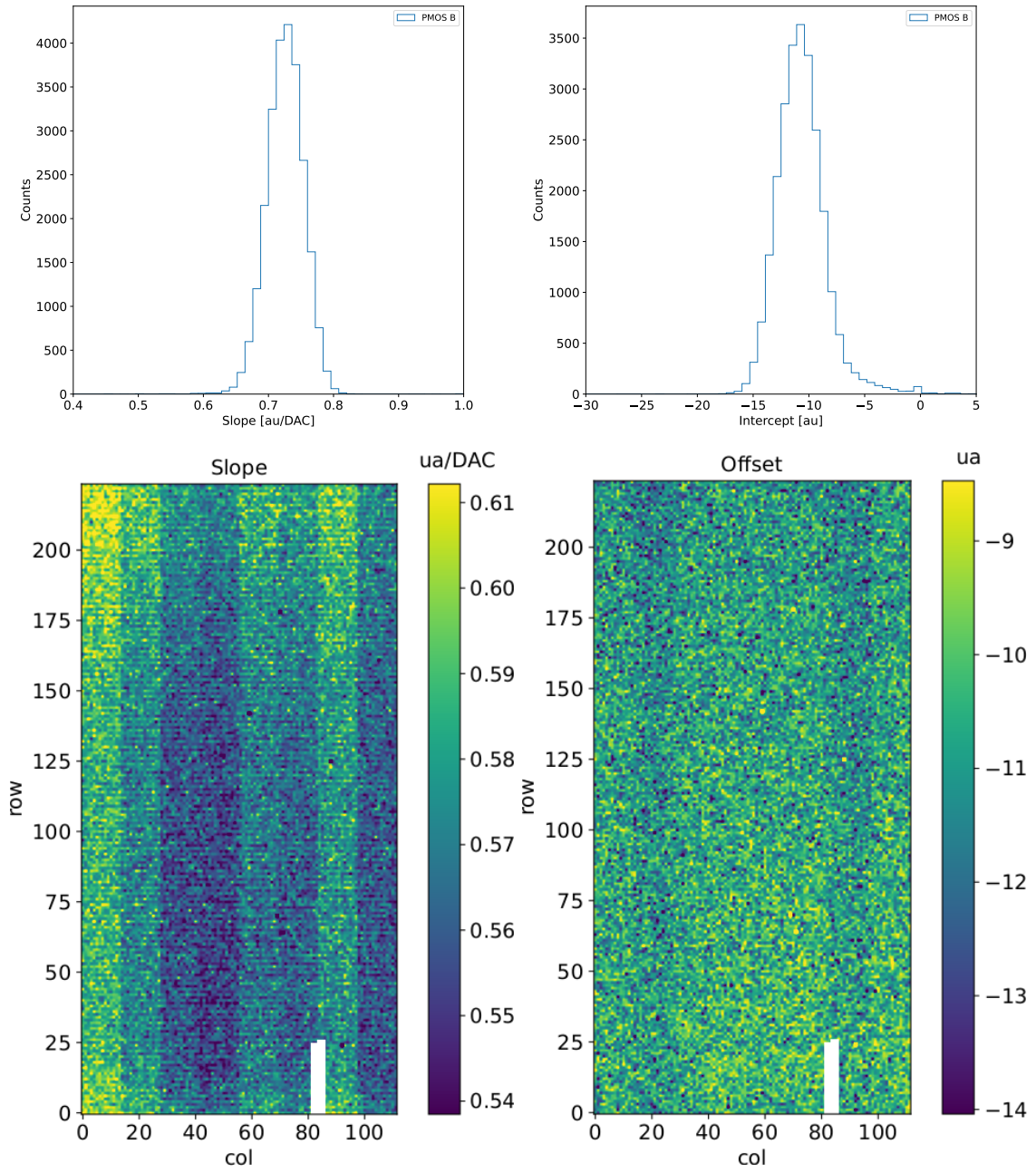


Figure 1.5: Histograms of the calibration parameters, slope (a) and offset (b), found fitting the ToT with a line, for the flavor B and with IDB fixed at 40 DAC. Maps of the calibration parameters, slope (a) and offset (b), found fitting the ToT with a line, with IDB fixed at 40 DAC.

167 respectively as:

$$K [e^- / DAC] = \frac{1616 [e^-]}{Q [DAC]} \quad (1.6)$$

168

$$C [F] = [e^- / DAC] \frac{1.6 \cdot 10^{-19} [C]}{14.7 [mV]} \quad (1.7)$$

169 where K is expected to be $20 e^- / DAC$, assuming the nominal value of C equal to $230 aF$,
170 and where 1616 is the expected number of electrons produced by the calibration source

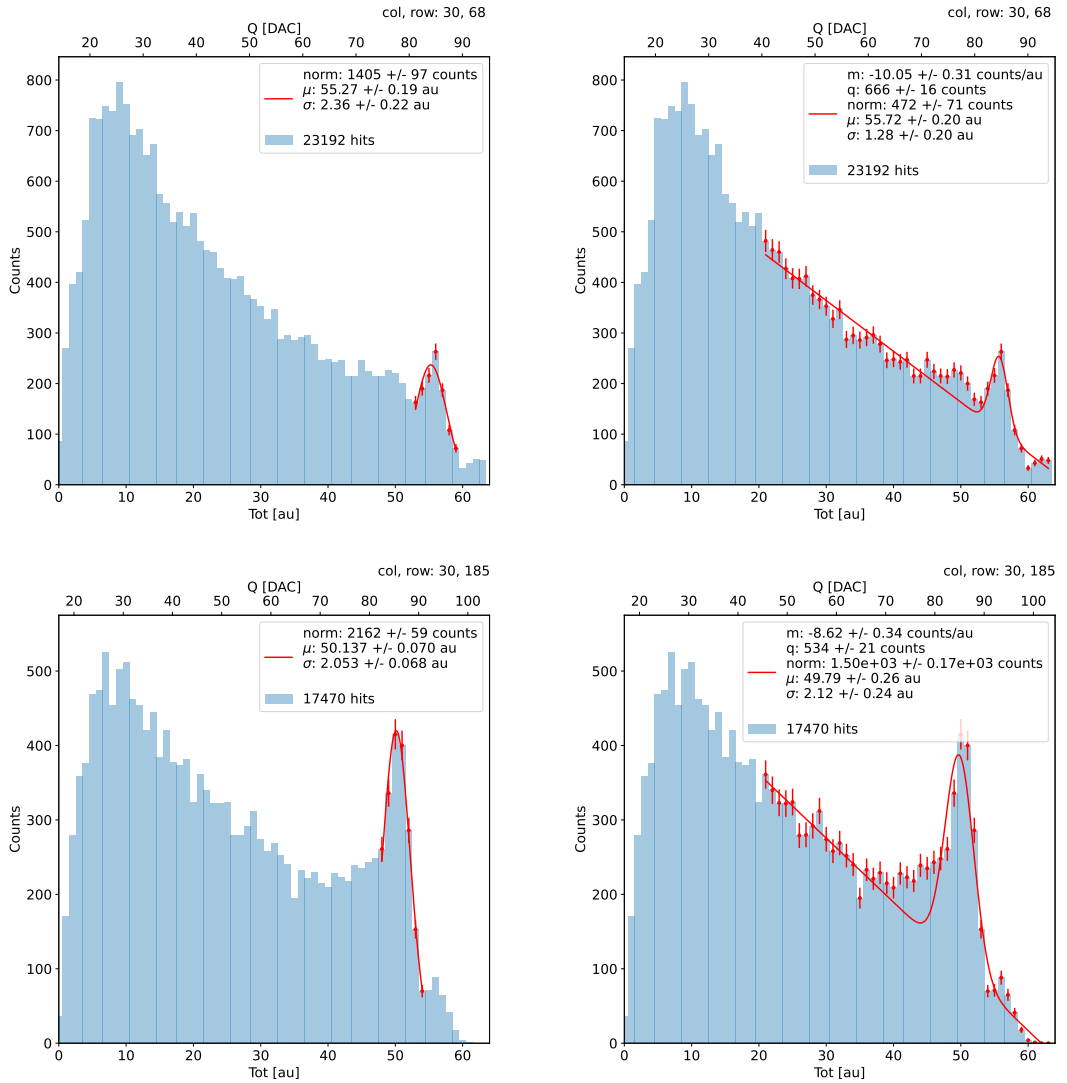


Figure 1.6: due pixel per far vedere la differenza tra i fit. Sottolinea che in rosso ci sono i bin fittati. La doppia scala utilizza le info trovate nel paragrafo precedente per il dato pixel in questione. Per avere una corrispondenza grezza in elettroni basta moltiplicare per 20 e- / dac.

171 used, Fe55. Fe55 is an extremely important radionuclide in the calibration of X-ray spec-
 172 trometers, proportional counter and scintillator detector since it emits two X-photons
 173 during the electron capture decay: the first one (K_{α}) at 5.9 keV and the second one (K_{β})
 174 at 6.5 keV. The K_{α} photon, which does photoelectric effect in silicon, has an absorption
 175 length $\lambda=7 \mu\text{m}$ to $8 \mu\text{m}$, and the probability of being absorbed in the $25 \mu\text{m}$ thick epitaxial
 176 layer is $\sim 0.95\%$. The electron emitted has an energy equal to the photon, so recalling
 177 that the mean energy needed to produce a couple electron-vacuum is 3.65 eV, the signal
 178 produced by the Fe55 source is expected to be 1616 e- . In figures 1.6 are shown two
 179 histograms of the ToT spectrum of the Fe55 source for two different pixels. The peak on
 180 the right corresponds to the events with complete absorption of the charge in the depleted
 181 region, while the long tail on the left to all the events with partial absorption due to charge
 182 sharing among neighbors pixels. In order to reduce the consistent charge sharing, the pixel
 183 dimension in TJ-Monopix2 has been reduced down to $30 \times 30 \mu\text{m}^2$. The events on the right

side of the peak, instead, corresponds to the K_β photons. Looking at the histograms for pixel (30, 185) and (30, 69) a significant difference in the peak to tail ratio leaps out, which can be related with the position of the pixel in the matrix. In particular, because of a different charge collection property, pixels in the upper part of the matrix (rows 112-224) have a more prominent peak, while in pixels in the lower part (rows 0-111) there is a higher partial absorption. Indeed, as discussed in section ??, there is a distinction in the structure of the low dose-epi layer among the rows, in particular pixels in rows 112-224, which have a RDPW, are supposed to have a higher efficiency in the pixel corner.

For the calibration I needed to establish the peak position; to do that I fitted the ToT histogram of each pixel. I tested two different fit functions:

$$f(x, N, \mu, \sigma) = \frac{N}{\sigma\sqrt{2\pi}} e^{-\frac{1}{2}(\frac{(x-\mu)}{\sigma})^2} \quad (1.8)$$

194

$$f(x, m, q, N, \mu, \sigma) = m x + q + \frac{N}{\sigma\sqrt{2\pi}} e^{-\frac{1}{2}(\frac{(x-\mu)}{\sigma})^2} \quad (1.9)$$

The additional linear term in equation 1.9 is meant to model the tail due to incomplete

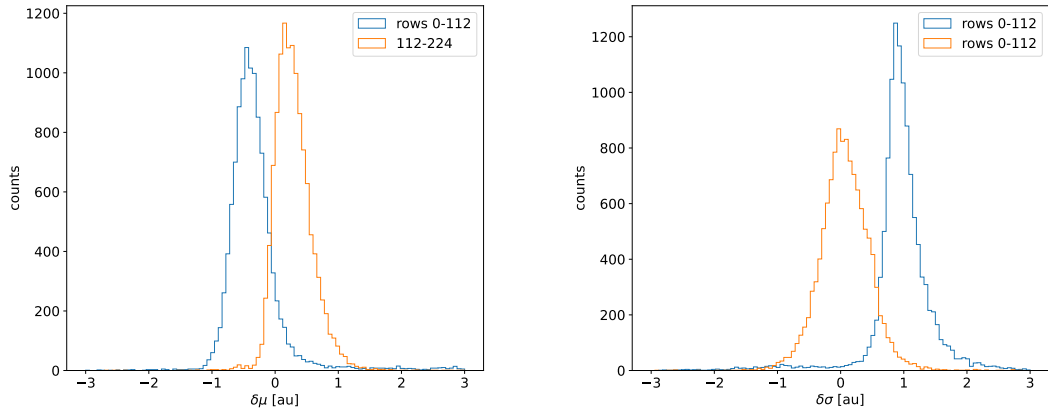


Figure 1.7: Difference between the parameters μ and σ obtained with the gaussian fit and those obtained with a gaussian plus a line. When $\mu < 0$ the fit with function 1.8 is generally worse (the peak is shifted to the left); when $\sigma < 0$, the fit with 1.9 is worse (larger sigma).

195

charge collection and prevent it from introducing a bias in the fitted peak position.

196 For this reason, when fitting with eq.1.9, I selected a larger region compared to the
 197 fit with eq.1.8, for which I used only a small reagion around the peak. The optimal fit
 198 region was chosen in both cases through an iterative routine: for the fit with eq.1.9 it
 199 starts from an interval including all the pixels above 20 DAC and progressively reduces it
 200 by increasing the left boundary; for the fit with eq.1.8, it starts from an interval of 5 bins
 201 around the expected peak position and reduces the interval of 1 bin at each iteration.

202 Even if the difference in the peak position between the two fit strategies is not really
 203 relevant for the purpose of the calibration, being of the order of 0.8-1.5% (1.7),it still
 204 introduces a systematic bias towards lower values due to the contribution of the tail.
 205 Indeed, we know that the sharp edge on the right must correspond to the case of complete
 206 absorption of the photon, so that, in general, the closest to this feature is the fitted peak
 207 position, the better the fit is. A poor fit tends also to overestimate the peak width. Even
 208

209 looking at the χ^2 , the fit function 1.8 seems to be the better choice, except for a sample
 210 of pixels in the lower part of the matrix, the one with lower efficiency.

211 The resolution of the detector, which is expected to be determined by the statistical
 212 fluctuations in the number of charge carriers generated in the detector as well as by the
 213 ENC, can be compared to the observed Fe55 peak width. Ideally:

$$\sigma_{Fe} = \sqrt{ENC^2 + F \times N} \quad (1.10)$$

214 Since the number of e/h pairs produced in the sensor is 1616, recalling that F for a silicon
 215 detector is 0.115 and that the ENC measured with the injection is 12e- , the σ_{Fe} is
 216 expected to be $\sim 18\text{e-}$. Looking at figure 1.8 the resolution achieved with the Fe55 source
 217 seems to be much higher. A contribution we have not taken into account but is certainly
 218 relevant is the systematic overestimation of the standard deviation of the Fe55 peak: this,
 219 as I already explained, is principally due to the high background of incomplete charge
 220 collection, which broadens the fitted peak.

221 2D maps of the value of the capacity and of the conversion factor found are shown in
 222 1.9. The evident stripe-structure in the matrix shows an evident correlation among the
 223 same row; the same structure, which is also visible in the slope map of the calibration of
 the ToT (fig.??), may be related with the structure of the bias lines.

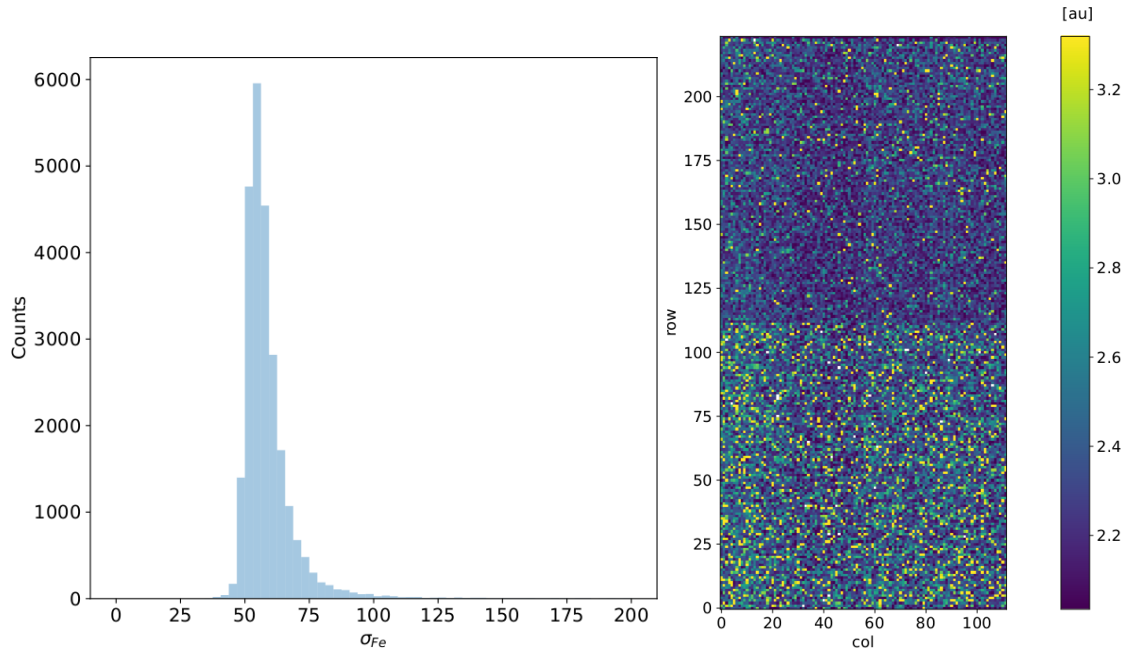


Figure 1.8: Histogram (a) and map (b) of the fitted Fe55 peak width.

224

225 HV flavor calibration

226 An attempt of calibrating the HV flavor, which is the most different from the PMOS B
 227 flavor, has been performed; however, because of the loss of signal caused by the higher
 228 capacity, we have been unable to identify the Fe55 peak in every FE and bias configuration.
 229 An example of Fe55 spectrum collected with the HV flavor is shown in figure 1.10.

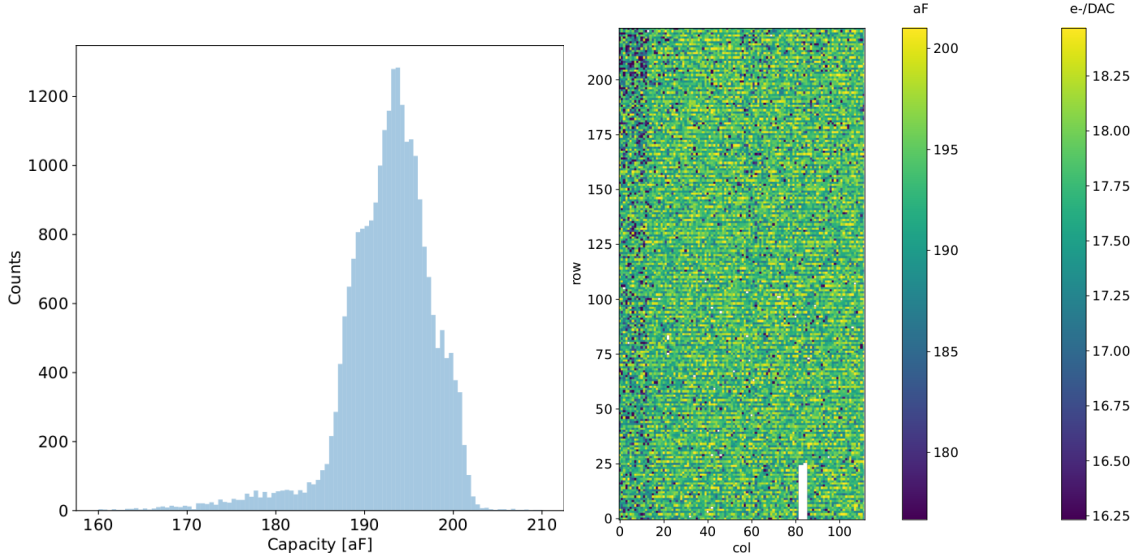


Figure 1.9: Histogram (a) and map (b) of the calibrated capacity of the injection circuit.

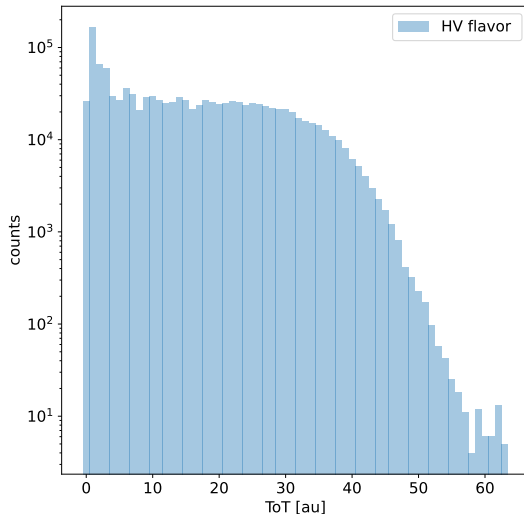


Figure 1.10: Fe55 spectrum with the HV flavor

230 1.1.4 Changing the bias

231 In order to study the behavior of the sensor as a function of the bias, I performed several
 232 injection scans in different configurations. Indeed, the thickness of the depletion region has
 233 to be considered an important parameters affecting the signal efficiency, and in particular
 234 it affects the charge released by a particle which crosses the sensor (since the signal is
 235 proportional to the thickness of the epitaxial layer). The measured output voltage ampli-
 236 tude and gain in the case of the PMOS and HV flavours are shown in figure 1.11 Given
 237 that the chip under examination has a gap in the low dose epi-layer, we were not able to
 238 change independently the bias of the substrate (PSUB) and of the p-well (PWELL), but
 239 they must be kept at the same value, differently from other chips of the same submission.
 240 Lowering the bias, the depletion region is expected to narrow and the efficiency to reduce,

	-6 V	-3 V	0 V
Threshold [DAC]	20.0 ± 1.6	21.0 ± 1.6	24.5 ± 1.8
Noise [DAC]	0.613 ± 0.075	0.625 ± 0.078	0.822 ± 0.098
Slope [au/DAC]	0.726 ± 0.027	0.707 ± 0.028	0.573 ± 0.021
Offset [au]	-10.8 ± 1.9	-11.2 ± 1.8	-11.1 ± 1.5

Table 1.2: The errors are the standard deviations of the corresponding distributions. The conversion factor from DAC to electrons is $\sim 20 \text{ e}^-/\text{DAC}$.

especially in the pixel corner, thus raising the threshold and the noise and decreasing the slope as a consequence of the reduction in the gain.

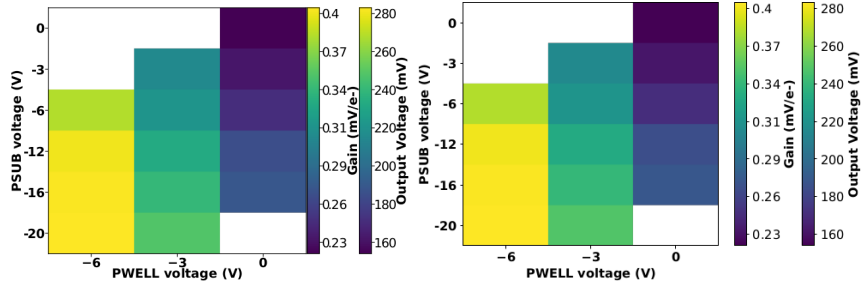


Figure 1.11: Output voltage amplitude and gain with respect to the p-well and p-substrate voltage in the case of the PMOS reset front-end (B)

In order to test the behavior of the chip when not completely depleted, I have performed an injection scan with PSUB/PWELL bias at 0 V, -3 V and -6 V (results in tab.1.2), and some acquisitions with the Fe55 source (fig. 1.12). There are reported the values of the K_α peak position, the normalization of the events above the peak and the rate, everything has been normalized to the value at the reference condition, which is with PSUB/PWELL at -6 V.

1.1.5 Measurements with radioactive sources

In order to completely validate the operation of the whole sensor¹, I have performed several acquisitions with radioactive sources, specifically Fe55 and Sr90Y, which is a β^- emittitor with electron endpoint at 2.2 MeV, and cosmic rays. I used the data collected with Sr90 and cosmic rays, to study charge sharing and events with more than one hit.

I define *cluster* the ensamble of all the hits with the same timestamp. This is obviously a coarse requirement, but it gave me the opportunity of using a simple and fast clustering algorithm, which is fine when the random coincidence probability is neglibile. Defining R_1 and R_2 as the two events rate, and τ as the dead time of the detector, the random coincidence rate can be found:

$$R_{coinc} = R_1 \times R_2 \times \tau \quad (1.11)$$

As I am going to prove in the next section, the dead time strictly depends on the occupancy of the matrix, even though we can assume a dead time of $\sim 1 \mu\text{m}$, which corresponds to

¹As I will discuss in chapter 2.2 these measurements serves also as a reference for the spectrum observed at the test beam

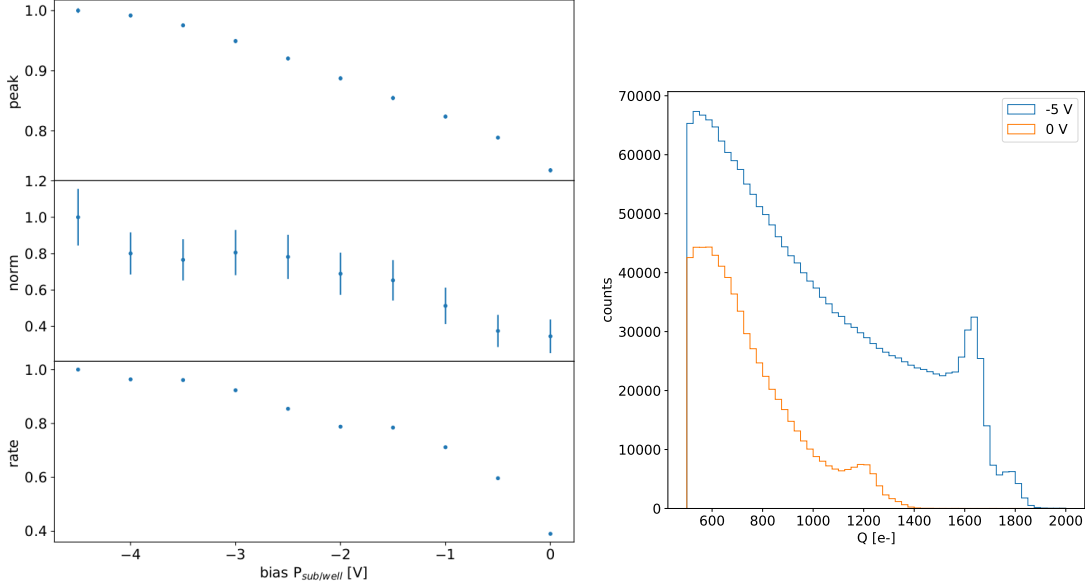


Figure 1.12: (a) Peak position, peak amplitude and rate as a function of the bias. Since during the collection of the whole data the source has been moved, it is not guaranteed that it has always had a repositioning in the same exactly place, then small the fluctuation of the rate along the decreasing trend are acceptable. The peak position and amplitude are estimated by fitting the spectrum with a gaussian in the region around the peak. (b) Fe55 spectrum at different $P_{sub/well}$ bias. The ToT values have been calibrated as explained in section. 1.1.3.

261 the mean dead time per pixel. However, if in an event a particle hits two different pixels
 262 producing a cluster, the total dead time simply doubles. Since the measured rate on the
 263 whole matrix of noise, Fe55, Sr90 and cosmic rays are \sim Hz, 3.3 kHz, 40 Hz and \sim 10 mHz²,
 264 the random coincidence probability are negligible except the one of two Fe55 events, which
 265 is 11 Hz.

266 In figure 1.13 I report the histograms of the number of pixels in the cluster and of the
 267 dimension of clusters, defined in terms of the max and min coordinates on the matrix as:

$$d = \sqrt{(y_{max} - y_{min})^2 + (x_{max} - x_{min})^2} \quad (1.12)$$

268 Looking at the shape of the histogram of the dimension, generally the Sr90 and the
 269 cosmic rays produce bigger clusters and hit a higher number of pixels, a trend that can
 270 be explained considering that the Fe55 photoelectron is much less energetic than the Sr90
 271 electron and cosmic rays. Below I have also attached a sample of hitmap of events produced
 272 by the three different sources (fig.1.14, 1.15).

273 In figures 1.18, 1.19, 1.21 are shown the distributions per different cluster dimension
 274 events, of the charge collected by a single pixel (figures on the left) and the charge collected
 275 by summing the charge collected by the pixels within the cluster (figures on the right).
 276 Since the noise rate is comparable with the cosmic rays and Sr90 ones, I have removed the
 277 single pixel events which are separately shown in figure 1.17; despite we cannot identify
 278 and selecting only the noise events, these distributions, and especially the cosmic rays
 279 one, are expected to be mostly populated by noise events. The distributions have a peak

²The cosmic rays rate at the sea level is expected to be \sim 1/cm²/s

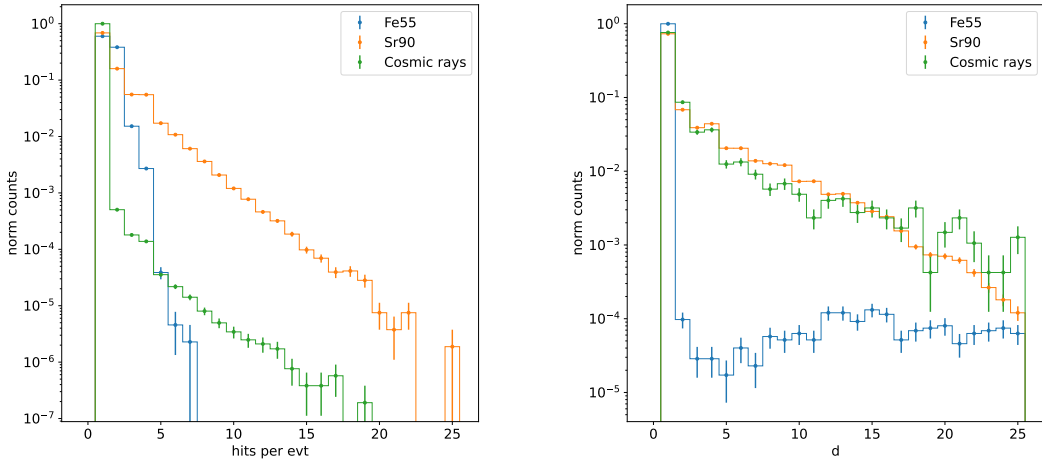


Figure 1.13: (a) Distribution of the number of hits per event with different sources. (b) Dimension of cluster defined as eq.1.1.5. Compared with the Sr90 and the cosmic rays, the Fe55 d distribution is characterized by a clear discontinuity in the cluster dimension. The very thin peak around 0 corresponds to the effective cluster, while the long tail at bigger cluster d is principally made of random coincidence.

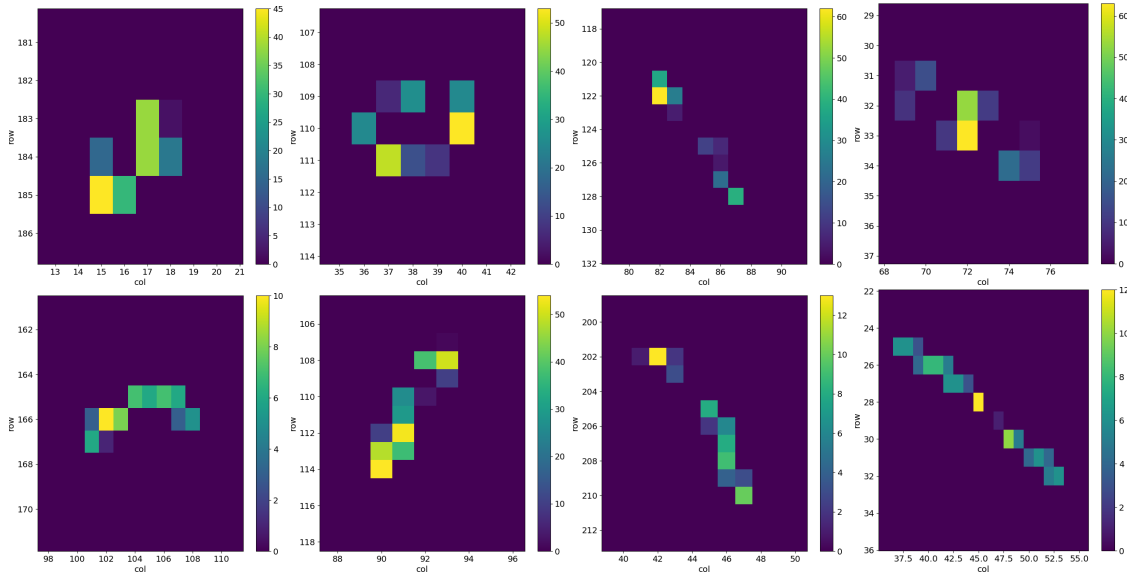


Figure 1.14: 2D histograms of the ToT in different events in an acquisition of cosmic rays.

280 around the threshold, which is compatible with the fact that the noise events typically
281 have a low ToT.

282 Looking at the spectra of Sr90 instead (fig:1.19), the maximum of the distribution of
283 the cluster charge seems to follow a linear dependence on the number of pixels hit (tab.1.3);
284 this can be accepted as a first approximation considering that the pitch ($36\text{ }\mu\text{m}$ and $40\text{ }\mu\text{m}$)
285 depending on the direction, and the epitaxial layer thickness ($25\text{-}30\text{ }\mu\text{m}$) are comparable.
286 However a more accurate model which takes into account the impact angle of the particle
287 should be developed for a more precise comparison. The charge per length covered Q/l
288 released by a particle which crosses more pixels and is not completely absorbed in the

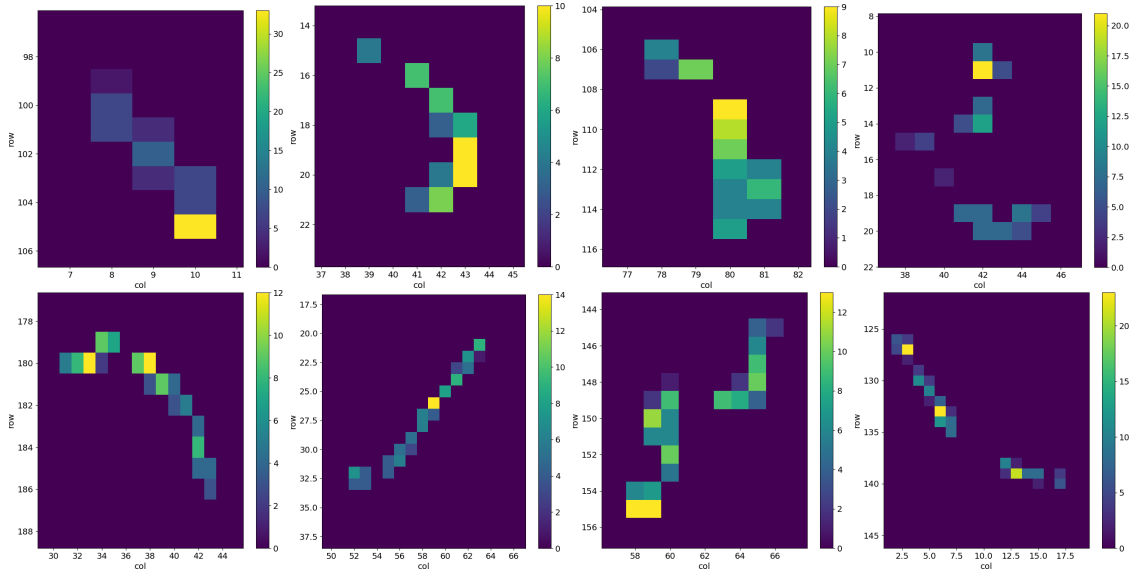


Figure 1.15: 2D histograms of the ToT in different events in an aquisition of Sr90.

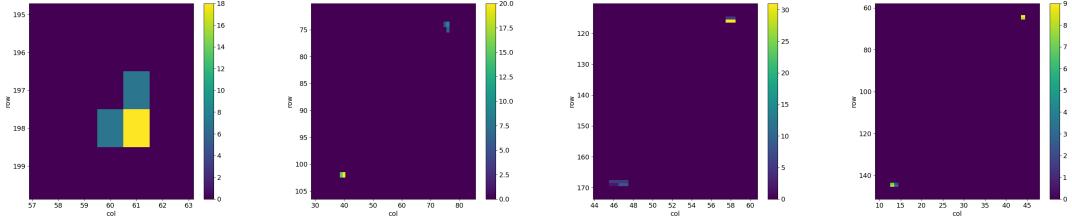


Figure 1.16: 2D histograms of the ToT in different events in an aquisition of Fe55

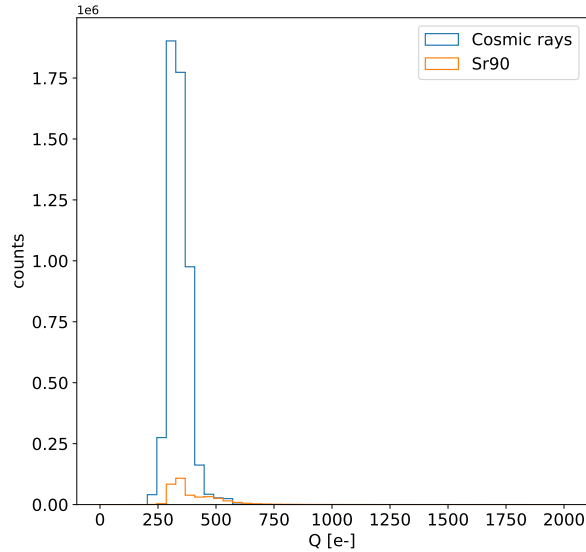


Figure 1.17: Histograms of the charge released in the pixels in events in which only a single pixel turns on.

Pixel per evt	Measured [e-]
2	950 ± 30
3	1450 ± 30
4	2050 ± 30
5	2450 ± 30

Table 1.3: Position of the maximum of the distributions in figure 1.19(b) of the summed charge released in the clusters depending on the number of pixel in the cluster.

²⁸⁹ sensor (fig.??) can be described by the following relation. Considering that:

$$l = \frac{t}{\cos(\lambda)} = \frac{t}{\sqrt{1 + tg^2\lambda}} = \frac{t}{\sqrt{1 + (x/t)^2}} \quad (1.13)$$

²⁹⁰ it can be expressed as:

$$\frac{Q}{l} = \frac{Q}{t} \sqrt{1 + (n - 1)^2 p^2 / t^2} \quad (1.14)$$

²⁹¹ where p/t is the ratio between the pitch and the epitaxial layer thickness, and then it
²⁹² is different in the x and y directions ($40 \mu\text{m}$ and $36 \mu\text{m}$ respectively). Taking as value of
²⁹³ p/t 1.52, which is the mean on the two axis, the value of Q/l expected by the scaling
²⁹⁴ relation and the charge actually measured in the acquisition with the Sr90 are illustrated
²⁹⁵ in table 1.3; because of the decision of cutting the single pixel events in order to have
²⁹⁶ a clean sample, the expected value has been obtained by the two hits cluster dividing
²⁹⁷ the charge by 2. By the inversion of the formula ??, the single pixel charge is then
²⁹⁸ expected to be 522 e-. FORSE DATO CHE LA MASSIMA CARICA RILASCIATA
²⁹⁹ SCALA LINEARMENTE CON IL NUMERO DI PIXEL NON SCRIVEREI QUESTA
³⁰⁰ COSA? O MAGARI LA METTO COME CORREZIONE? The measured value has been
³⁰¹ obtained by the maximum of the distributions in the left plots in ??

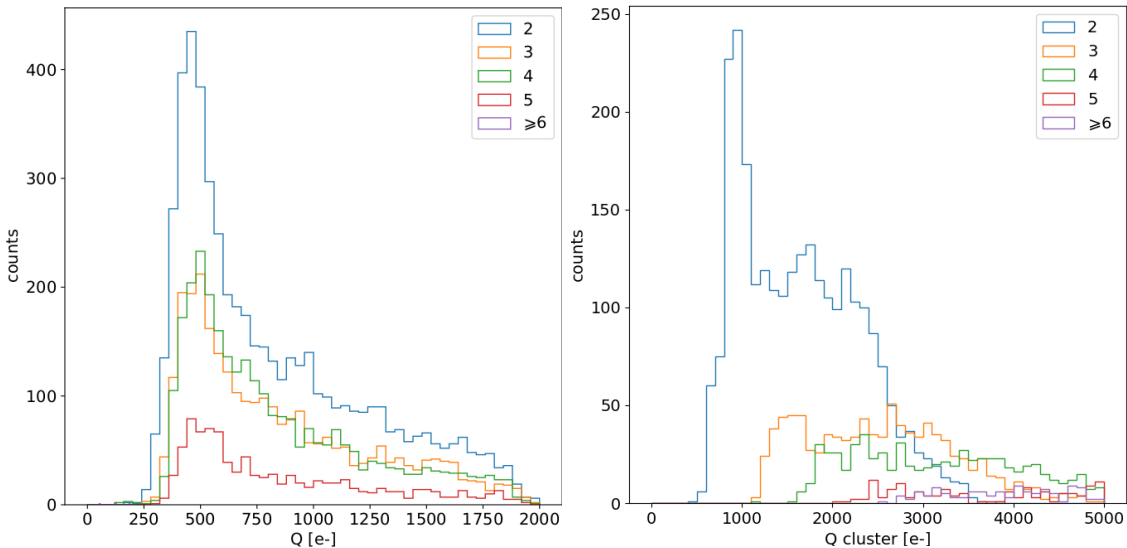


Figure 1.18: Acquisition of cosmic rays with IDB=40 DAC

³⁰² Regarding the Fe55, the bump in the cluster spectrum at $\sim 1616 \text{ e-}$ corresponds to
³⁰³ photons which had converted at the boundary of nearby pixels thus sharing their charge
³⁰⁴ among them. Starting from 4-pixels clusters the peak moves to the right: this is due to

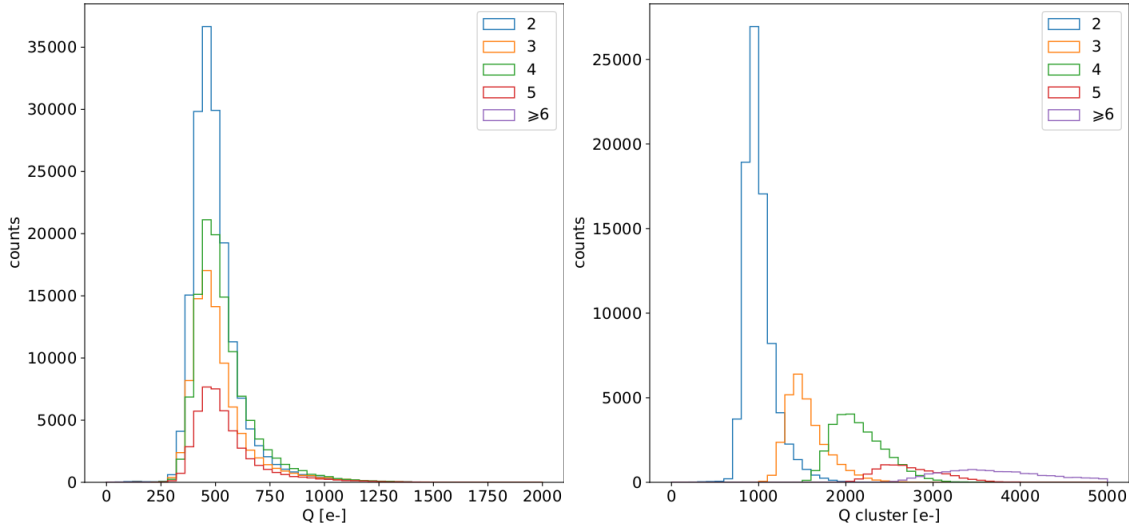


Figure 1.19: Acquisition of Sr90 with IDB=40 DAC

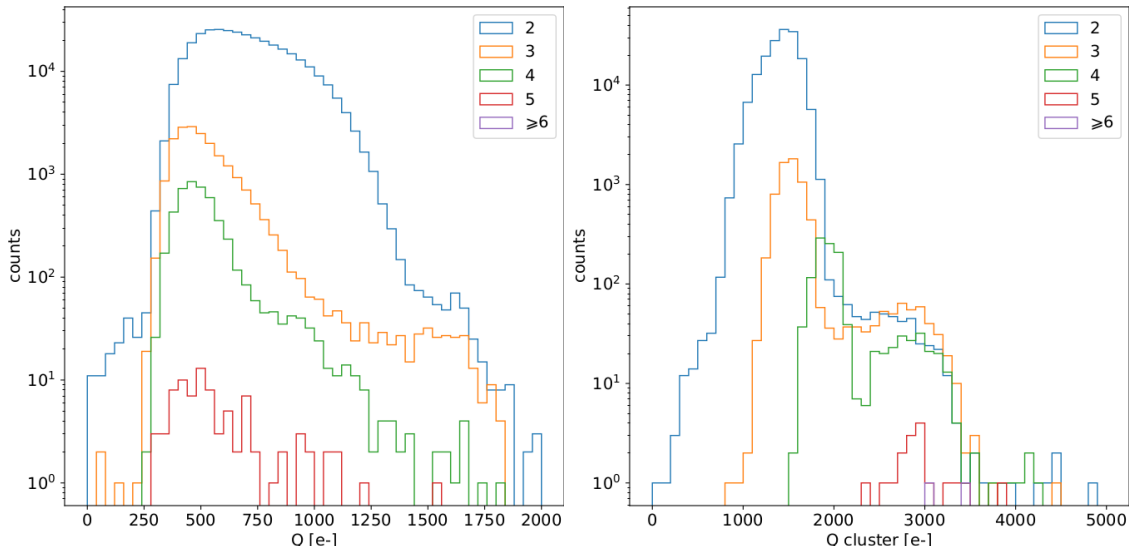


Figure 1.20: Acquisitions with radioactive source and cosmic rays at IDB=40 DAC.

Figure 1.21: Acquisition of Fe55 with IDB=40 DAC

the fact that the cluster with more than 3 pixels are principally random coincidence events Fe55-Fe55 or Fe55-noise. Recalling that the noise typically just exceeds the threshold and then has low ToT, the peak position in the spectrum ?? of 4-pixel cluster can be explained admitting that one of the four pixel is a noise signal. The shoulder on the right, instead, which have an edge at about 3200 e- corresponds to the events with coincidence of two photons. Looking at the charge on the single pixel spectrum (fig.??), instead, a small bump can be seen around 1616 e-: these events correspond to photons which released almost all the charge on one pixel.

1.1.6 Dead time measurements

The hit loss is due to analog and digital pile up: the first one occurs when a new hit arrives during the pre-amplifier response, the second instead when the hit arrives while

316 the information of the previous hit has not yet been transferred to the periphery. Since the
 317 pre-amplifier response has a characteristic time \sim ToT, the dead time τ_a introduced by it
 318 will be at most 1.6 μ s; using the IRESET and VRESET FE parameters the reset time can
 319 be lowered down, but as explained in section ?? it must be longer than the preamplifier
 320 characteristics time in order to not cut the signal. Regarding the latter contribution instead,
 321 since only one hit at a time can be stored on the pixel's RAM, until the data have completed
 322 the path to get out, the pixel is paralyzed. Moreover since there is no storage memory
 323 included on TJ-Monopix1 prototypes, the digital dead time τ_d almost corresponds to the
 324 time needed to trasmit the data-packets off-chip.

325 The exportation of data from pixel to the EoC occurs via a 21-bits data bus, therefore
 326 only one clock cycle is needed and the dead time bottleneck is rather given by the
 327 bandwidth of the serializer which trasmits data off-chip from the EoC. In our setup the
 328 serializer operates at 40 MHz, thus to transmit a data packet (27-bit considering the ad-
 329 dition of 6 bits to identify the double-column at the EoC) at least 675 ns are needed. For
 330 what we have said so far, the R/O is completely sequential and therefore is expected a
 331 linear dependence of the reading time on the number of pixels to read:

$$\tau = 25 \text{ ns} \times (\alpha N + \beta) \quad (1.15)$$

322 where α and β are parameters dependent on the readout chain setting.

323 To test the linearity of the reading time with the number of pixels firing and to measure
 324 it, I have used the injection circuit which allows me choosing a specific hit rate: I made
 325 a scan injecting a fix number of pulses and each time changing the number of pixels
 326 injected. Indeed the injection mode allows fixing not only the amplitude of the pulse,
 327 which corresponds to the charge in DAC units, but also the time between two consecutive
 328 pulses (DELAY). The hit rate then corresponds to 25 ns/DELAY.

329 Unfortunately a high random hit rate on the matrix cannot be simulated by the in-
 330 jection because of the long time (\sim ms) needed to set the pixel registers of the injection;
 331 then I was forced to specify at the start of the acquisition the pixels to inject on, and for
 332 convenience I chose those on a same column. In figure 1.22 is shown the dependence of
 333 the efficiency on the DELAY parameter in two different cases. For the 5 pixels example
 334 the efficiency goes down the 90% at a DELAY of \sim 185 clock counts, which corresponds
 335 to 4.625 μ s and to a rate of 216 kHz, while in the 10 pixels example, the efficiency goes
 336 under the 100% at \sim 380 clock counts, which corresponds to 9.5 μ s and to a rate of 105 kHz.
 337 From the efficiency curves I have then looked for the time when the efficency decreases.
 338 In figure 1.23(a) is shown the dead time per pixels as a function of N with different R/O
 339 parameters configuration, the meaning of which is explained in chapter ???. The default
 340 value suggested by the designer of the chip are reported in table 1.4; moving too much
 341 the readout parameters from the default ones, the readout does not work properly, and no
 342 hits can be read at all. The problem probably stays in the firmware setting of the readout
 343 which are specially fixed for our chip **Sul repository, nei commenti ci sono altri valori pos-
 344 sibili per il FREEZE, ma avevamo detto che probabilmente sono relativi ai setting di altri
 345 chip.** Despite the single pixel reading time does not depend on the position on the pixel
 346 matrix, whithin a clock count which is \sim 25 ns, and it is equal to 106 clock counts, since
 347 the τ_d critically depends on the pixel position on the matrix: in particular the reading
 348 sequence goes from row 224 to row 0, and from column 0 to column 112, making the pixel
 349 on the bottom right corner the one with the longest dead time.

350 Furthermore to test that there is no dependece of the digital readout time from the

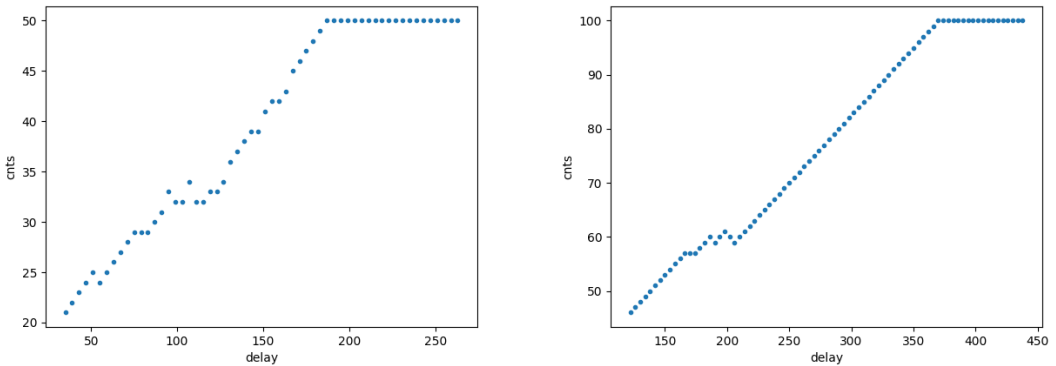


Figure 1.22: Efficiency vs the DELAY parameters. (a) I made a scan injecting 5 pixels with 50 pulses for each DELAY configuration and (b) 10 pixels with 100 pulses for each DELAY

Parameter	Value [DAC]	Value [μ s]
START_FREEZE	64	1.6
STOP_FREEZE	100	2.5
START_READ	66	1.65
STOP_READ	68	1.7

Table 1.4: Default configuration of the R/O parameters

charge of the pulse, I have try to change the amplitude of the pulse injected, but the parameters found were consistent with the default configuration ones. No difference in the α and β coefficients has been observed between the two case. Referring to eq.1.15, the factor α is proportional to the difference (STOP_FREEZE - START_READ), while the offset β lies between 5 and 15 clock counts.

The readout time found by this test is so long because in the prototypes no parallelization of the informations (with the instruction of more serializer for example) and no storage memory are included; this feature are typically added in the final prototypes. An example closely linked to TJ-Monopix1 is OBELIX: it will include on the chip a storage buffer to optimize the dead time and to keep a low occupancy even at high fluence.

1.2 ARCADIA-MD1 characterization

Unfortunatly the characterization of MD1 has not yet been completed because of some problems with the functionality of the first chip we received on which we have been able to make only a few electrical and communication test in order to test the operations of the FPGA and the breakount board (BB). We asked for another chip then but we, due to delay in the extraction and the bonding of the wafer, have received it one week ago; an exhaustive characterization and testing of the new chip have been going on in the clean room on the INFN, and I am going to show here only some preliminary results.

The problem with the broken chip occurs when it is biased, in particular, when the HV voltage is lowered down 0V, the sensor requires too much power and a too high current draw sets. We have discussed the problem with the designers of the chip whose helped

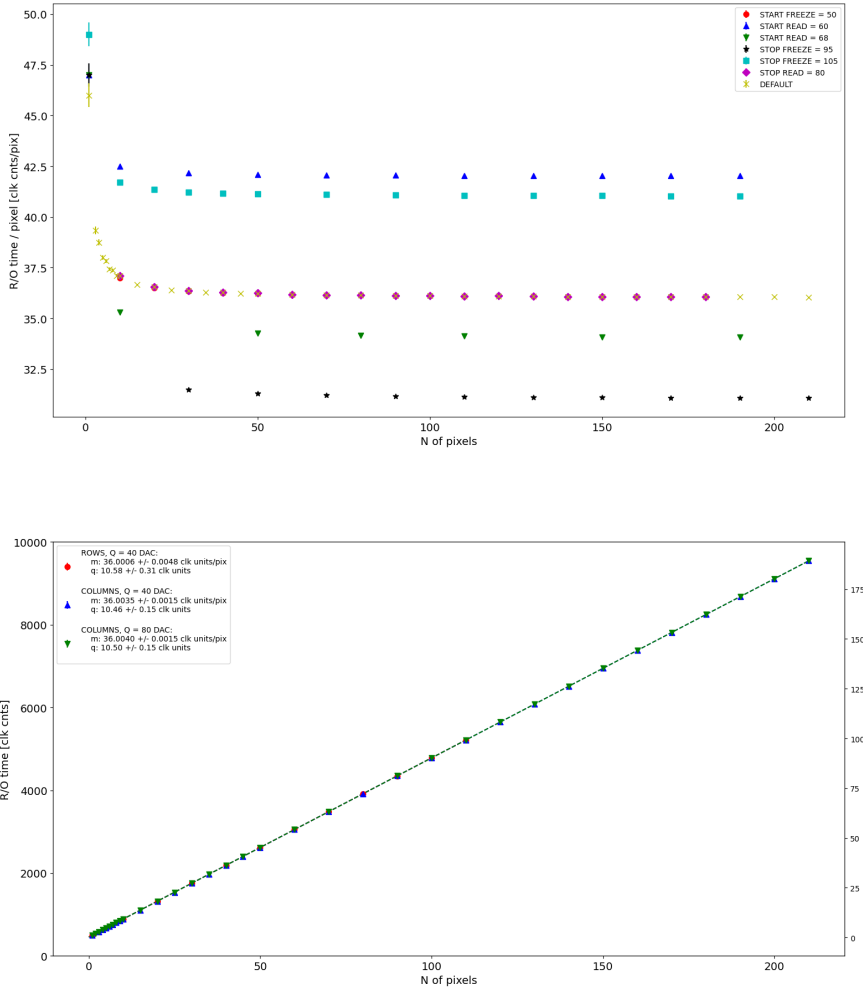


Figure 1.23: (a) Readout time per pixel as a function of the number of pixel injected obtained with different FE setup. (b) Readout time as a function of the number of pixels injected obtained injecting pulses with amplitude of 80 DAC (green), of 40 DAC on the same row (red) and on the same column (blue).

us indentifying the motivation of the break: the chip has been glued using too much conductive tape and hence have a short-circuit between the sides and the back, which makes impossible the biasing. Unfortunately, since both the sensor and the FE require at least -10 V to work properly, no measurement was possible except the acquisition of the noise in the FE circuit.

The second chip we received is a minid2, that is a "mini demonstrator" from the second submission. The two have the same charateristics but the minid2 is smaller than the MD1, in particular it only have 32×512 pixels, instead of 512×512 .

Up to now we used the injection circuit in order to make a threshold scan on a few pixels: differently from the TJ-Monopix1's charaterization where we performed a scan changing the injection charge of the pulse, with the minid2 we have instead changed the threshold (whose register is VCASN) keeping the charge of the pulse fixed. For each threshold we inject 100 pulses of amplitude $10 \mu\text{s}$. The dependence of the efficiency on the threshold for two pixels is shown in figure 1.25. Even if the behavior is reasonable, as the

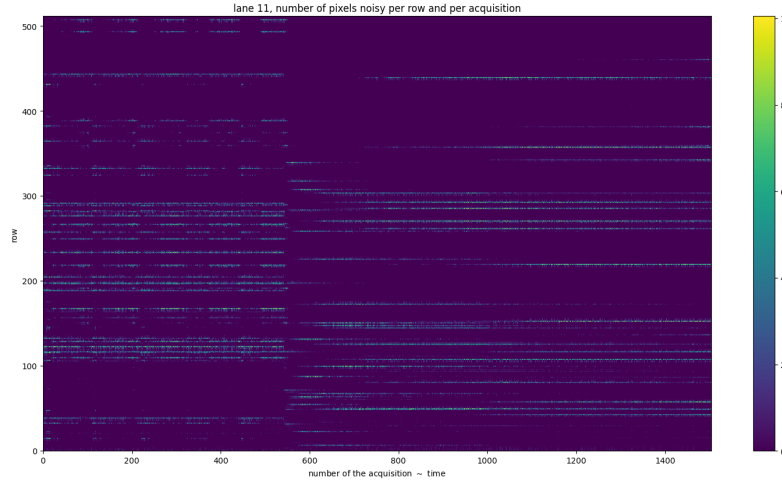


Figure 1.24: Noise in the front end circuit depending on the bias road across the matrix was recorded.

396 threshold is reduced the efficiency becomes higher, it is possible that the bias (-50 V) is not enough to full deplete the sensor, since the counts does not reach the 100% steadily.

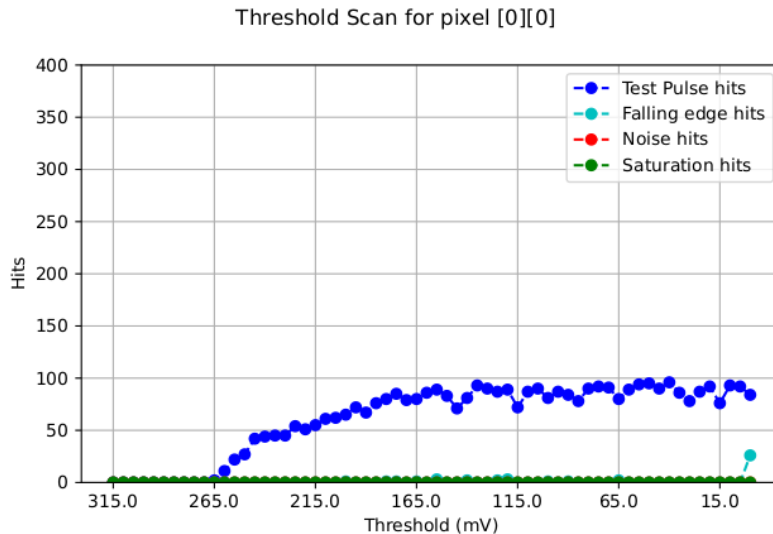


Figure 1.25: Threshold scan on the pixel (0,0). The sensors is polarized with $\Delta V = -50$ V.

397
398 The value of the SNR and the ENC Charge injection circuit uses $C_{inj} = 2.325$ fF The
399 SNR, the ENC and the threshold dispersion on the matrix are expected to be respectively
400 ~ 90 , $3 e^-$ and $\sim 35 e^-$ with a detector capacity of 7 fF, that is about the capacity expected
401 for the detector. The injection capacity is expected to be ~ 2.325 fF, and in this condition
402 the the minimum and maximum signals generated are respectively 0.08 fC and 2.6 fC.

403 Substantial differences have been observed with VCASN=40 DAC in both the efficiency
404 and the threshold among the sections; this suggests that with this particular FE config-
405 uration there is a big threshold dispersion on the matrix. The hitmap of an acquisition
406 with the Fe55 source is shown in figure 1.26: the whole MD1 matrix with only the bottom
407 region (32 rows) working is represented in (a), while in (b) there is a zoomed hitmap. The

408 rate seen within the region 8 (green region in the figure (a)) is compatible with the rate
of the same radioactive source measured with TJ-Monopix1, that it ~ 3.3 kHz. Looking to

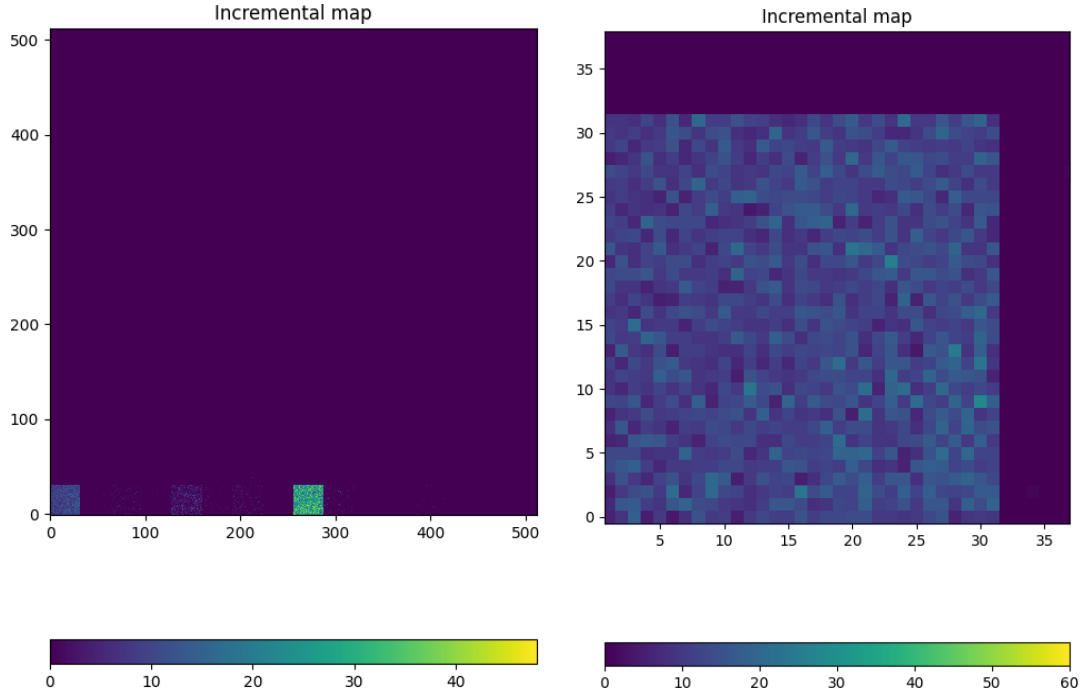


Figure 1.26: Fe55 acquisition with VCASN=40 DAC. (a) All the matrix 512×512 is plotted even if the minid2 has only the rows in range 0-32. (b) A zoom on the first section (col 0-32).

409
410 the Sr90 acquisitions (fig.1.27) many clusters and tracks can be immidiately distiguished,
confirming what observed with TJ-Monopix1.

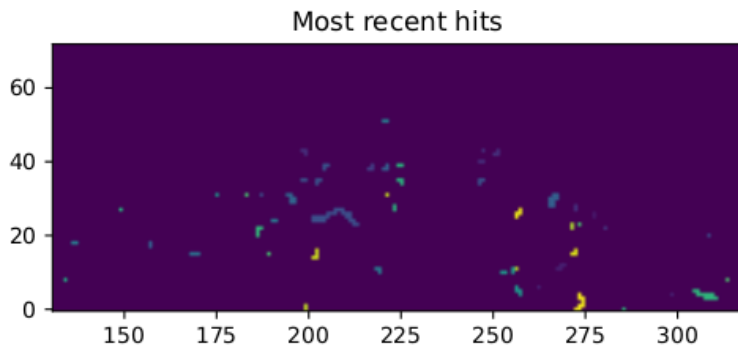


Figure 1.27: Sr90 acquisition with VCASN=40 DAC. The different colours are related with the time of arrival of the hits: in yellow the most recent hits, while in blue the old ones.

411

⁴¹² **Chapter 2**

⁴¹³ **Test beam measurements**

⁴¹⁴ During August 2022 a testbeam took place in Santa Chiara hospital in Pisa, where a
⁴¹⁵ new accelerator designed for both medical research and R&D on FLASH-RT, and for this
⁴¹⁶ reason called "ElectronFlash", have been installed a few months ago. The motivation
⁴¹⁷ of the testbeam measurements were testing TJ-Mopopix1 at high dose rate with a focus
⁴¹⁸ on investigating the possibility of the application in radiotherapy. Despite this particular
⁴¹⁹ device does not seem fitting the requirements imposed for that application, especially
⁴²⁰ regarding the readout time, the measurements have been useful since help us characterizing
⁴²¹ the setup for future advance, and also give us the possibility of a complete characterization
⁴²² of the chip.

⁴²³ Given that in medical physics the dose is the standard parameter to characterize the
⁴²⁴ beam, because of its obvious relation with the damage caused in the patient, I am going
⁴²⁵ to explain the meaning of it by the point of view of the instrumentation. Infact, when
⁴²⁶ interacting with measuring systems a more common and useful parameter is the rate or
⁴²⁷ the fluence of particles. The conversion between the two quantity can be found thinking to
⁴²⁸ the definition of dose: it is the concentration of energy deposited in tissue as a result of an
⁴²⁹ exposure to ionizing radiation. Assuming total absorption of electrons in water, defined
⁴³⁰ by law as the ordinary reference medium, the dose can be expressed as:

$$D[Gy] = \frac{NE[eV]}{\rho[g/cm^3]A[cm^2]x[cm]} \quad (2.1)$$

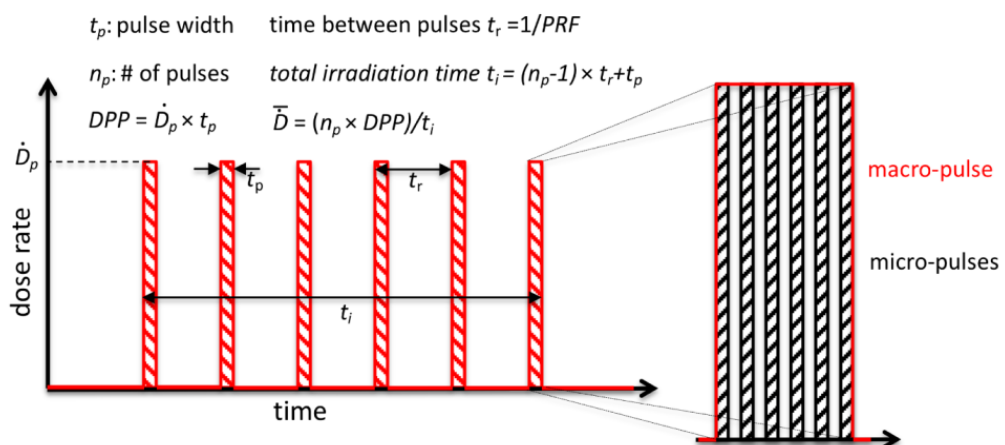


Figure 2.1: Typical beam structure of a beam used in electron radiotherapy

\bar{D}	Dose rate (mean dose rate for a multi-pulse delivery)	0.005-10000 Gy/s
\dot{D}	Intra pulse dose rate (dose rate in a single pulse)	0.01-1 10^6 Gy/s
DDP	Dose in a single pulse	0.04-40 Gy
PRF	Pulse repetition frequency	1-350 Hz
t_p	Pulse width	0.2-4 μ s
n	Number of pulses	single/pulse train

Table 2.1: The parameters that can actually be set by the control unit are the PRF, DDP, t_p and n (in particular the modality of singular irradiation or pulse train), while the other changes consequently.

431 After having applied the conversion of the energy from eV to J and noticed that $E/\rho x$
 432 roughly corresponds to the stopping power S of electrons in water, a simple estimation of
 433 the dose released in water is:

$$D[Gy] = 1.602 \cdot 10^{-10} N[cm^{-2}] S[MeV cm^2/g] \quad (2.2)$$

434 2.1 Apparatus description

435 In order to shield the outdoor from ionizing radiation the accelerator is placed in a bunker
 436 inside the hospital. The bunker has very thick walls of cementum and both the control
 437 units of the accelerator and of the detector were placed outside in a neighbor room.

438 2.1.1 Accelerator

439 The ElectronFlash accelerator is an electron Linear Accelerator (LINAC) with two energy
 440 configurations, at 7 MeV and 9 MeV, and it can reach ultra high intensity (40 Gy/pulse)
 441 keeping the possibility of accessing many different beam parameters and changing them
 442 independently from each other, a characteristic that makes it almost unique worldwide
 443 and which is fundamental for research in FLASH-RT, both for the medical aspects¹ and
 444 for the studies on detectors. The accelerator implements the standard beam structure
 445 used in RT with electrons (fig. 2.1), that is a macro pulse divided in many micropulses;
 446 the parameters used to set the dose and their range of values settable by the control unit
 447 is reported in table 2.1.

448 The accelerator is also provided of a set of triod cannons ~ 1.2 m long and with diameters
 449 in range from 1 cm to 12 cm and a collimator that can be used as beam shaper to
 450 produce a squircle shape. The triode, which is made by plexiglass, must be fix to the gun
 451 during the irradiation and is needed for producing, via the scattering of electrons with it,
 452 an uniform dose profile (fig.2.2) which is desired for medical purpose.

453 2.1.2 Mechanical carriers

454 The tested detector consists in one chip, the Device Under Test (DUT), mounted on
 455 a board and connected to FPGA with same arrangement of figure ???. These boards
 456 have been positioned vertically in front of the triode on a table specifically built for the

¹For example, it is not yet really clear the dependence of the efficacy of the FLASH effect on the whole beam parameters

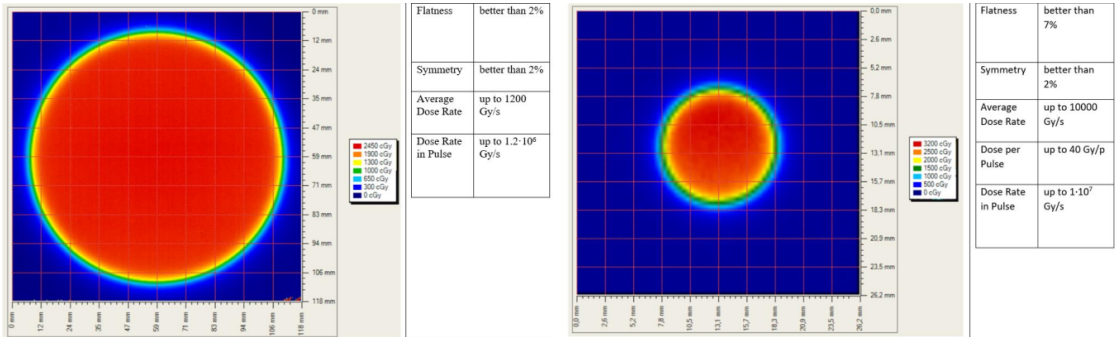


Figure 2.2: Two example of x-y isodose curves for two different triodes, 10 cm and 1 cm respectively, reported by the producer in the manual with the specific of the accelerator (S.I.T. - Sordina IORT Technologies S.p.A.). With the smaller collimator the dose rate in pulse is comparatively higher.

457 testbeam. The tree board have been enclosed in a box of alluminium with a window on
 458 the DUT and with the required holes at the side to enable the biasing via cables and the
 459 connection with the DAQ provided via ethernet cable. A trigger signal coming from the
 460 control unity and syncronized with the pulses emitted from the beam has been also sent to
 461 the FPGA. This digital signal cannot be considered a real trigger, since the TJ-Monopix1
 462 prototype has been designed to be triggerless, but its Time of Arrival (ToA) had allowed
 463 the reconstruction of the correct timing during the analysis.

464 In order to shield the sensor from the whole particles emitted from the gun, two
 465 alluminium collimators have been fabricated: one has been positioned at the triode exit
 466 while the other in front of the DUT. The collimators are $t=32$ mm thick and have a
 467 diameter d equal to 1 mm: assuming a beam divergence bigger than $d/t=1/32 = 1.8^\circ$,
 468 which is the case, the collimator at the triode output was supposed to work as a point
 469 source and to reduce the rate on the DUT of a factor at least $4 \cdot 10^{-4}$. The second one,
 470 being near the DUT, was instead supposed to shield the sensor from the electrons which
 471 have passed the first one, except for a region of 1 mm^2 configurable using **come si chiamano**
 472 **quei cacciavitini per settare la posizione? sliding trimmer?**.

473 2.2 Measurements

474 Because of the dead time of TJ-Monopix1 it is not possible resolving the bunch sub-
 475 structure and almost no one pixel can read more than a hit per bunch. I recall, indeed,
 476 that the dead time per pixel depends on the location on the readout priority chain and
 477 for each pixel $\lesssim 1 \mu\text{s}$ are needed; therefore, assuming a pulse duration of $4 \mu\text{s}$, only a few
 478 pixels at the top of the priority chain (placed at the upper left on the matrix) can fire a
 479 second time, as they can be read a first time before the end of the pulse and then can be
 480 hit again.

481 Since resolving the single electron track is impossible, a way this sensor could be used
 482 in such context is reducing its efficiency and taking advantage of the analog pile up and
 483 of the linearity of the analog output (ToT), in order to see a signal produced not by the
 484 single particle but by more electrons. Reducing the efficiency and the sensibility of the
 485 sensor is essential in order to decrease the high charge signal produced in the epitaxial
 486 layer and mitigating the saturation limit: the smaller the output signal produced by a

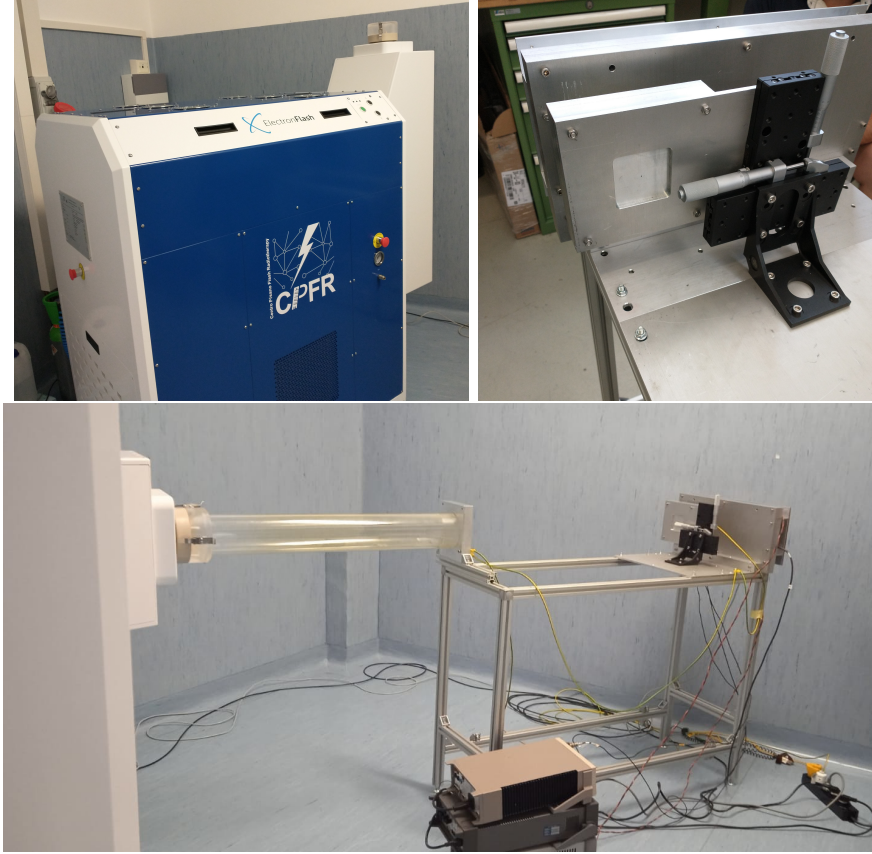


Figure 2.3: Experimental set up. (a) ElectronFlash accelerator: a rotating gantry allows the gun orientation from 0° to 90° (horizontal /vertical). (b) Collimator and DUT box. (c) Whole structure mounted: we used the 10 cm diameter and 1.2 m long triode; the DUT which is in the box behind the two collimators is connected to the power supply units.

487 particle and the higher the fluence the detector can cope with. There is an obvious limit in
 488 this context that is the ToT rollover, indeed, the signal stop giving information when this
 489 value has been overridden and is no more bijective. With the standard configuration of
 490 the FE parameters and the epitaxial layer completely depleted, a MIP produces a charge
 491 at the limit of representation with a 6-bit ToT; to obtain smaller output signals one can
 492 operate on the reduction of the gain.

493 Recalling the results in section 1.1.4, I have shown that concerning the PMOS flavor
 494 B, reducing the bias from -6 V to 0 V brings a reduction of efficiency down to 40 %, and a
 495 reduction in the gain of a factor $\sim 1/3$, while the reduction of the gain of the preamplifier
 496 allows a reduction of **circa 10, ma da controllare**.

497 In order to take advantage of the analog pile up and integrating the charge, for
 498 simplicity assume of two electrons, the second one must hit the pixel before the ToT goes
 499 under the threshold. The general condition is then $\overline{\Delta T} < \overline{ToT}$, but if a high $P_\mu(n \geq 1)$ is
 500 required, a lower $\overline{\Delta T}$ may be desired:

$$P(n \geq 1) = \sum_{n=1}^{\infty} \frac{e^{-\mu} \mu^n}{n!} = 1 - P(0) = 1 - e^{-\mu} \quad (2.3)$$

501

$$\mu = \frac{\overline{ToT}}{\overline{\Delta T}} \quad (2.4)$$

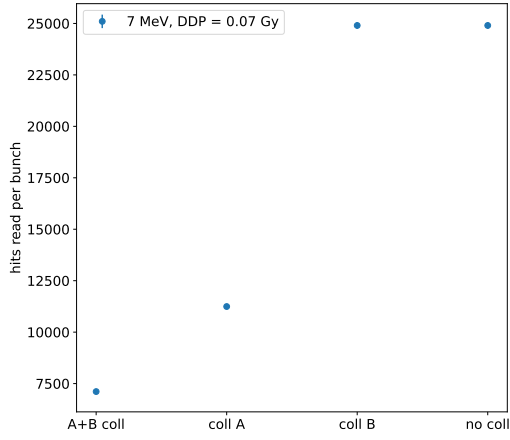


Figure 2.4: Mean number of hits read per bunch at DDP=0.07 Gy, with all the possible setup condition: with both the collimator, with only the collimator far from the chip (A), with only the collimator near the chip (B), and without any collimator.

502 If a $P_\mu(n \geq 1) = 99\%$ then the $\overline{\Delta T}$ must be $\sim 0.22 \overline{ToT}$. The ToT is in range [0,64] but
 503 since the rollover must be avoided, the \overline{ToT} must be lower than 32, and then the minimum
 504 rate on the pixel must be 1.25 MHz.

505
 506 During the testbeam many runs have been performed, spanning the energy, the dose
 507 per pulse and the four possible configurations with/without the collimators. We have
 508 collected data with the PMOS flavor A in the standard configuration: with the PWELL
 509 and PSUB biased at -6 V and set the standard default FE parameters reported in table
 510 ???. During all the data acquisitions we have selected on the control unit of the accelerator
 511 pulses with t_p of 4 μ m and with the smallest PRF settable, which is 1 Hz, in order to start
 512 in the most conservative working point excluding the digital pile up of events from different
 513 bunches. In these conditions, even if the whole matrix turns on, the total readout time
 514 corresponds to $25000 \times 1 \mu s = 25 \text{ ms}$ is still lower than the time between two consecutive
 515 pulses. In figure 2.4 is shown the mean number of hits read during one accelerator pulse
 516 in different setup conditions.

517 The readout starts with the trailing edge of the first pulse going down the threshold:
 518 about 50 clk=1.25 μ s after this moment the FREEZE signal is sent to the whole matrix,
 519 and the transmission of the data to the EoC begins. The hits read during the FREEZE
 520 signal are the ones whose TE occurred before the start of the FREEZE and which have the
 521 TOKEN signal high; the ones, instead, whose TE occur during the FREEZE are stored in
 522 the pixel memory until the end of the FREEZE. At this point a second readout starts and
 523 a second FREEZE is sent to the matrix. An example of the two sub-pulses corresponding
 524 to an electron bunch is shown in figure 2.5: in the acquisition we injected 5 pulses with
 525 both the collimators mounted on the table. Looking at the spectrum we can see that the
 526 second sub-pulse has a populated tail on the right; this is due to the fact that the hits
 527 which arrive before the start of the first FREEZE but have a long ToT that falls during
 528 the FREEZE, are read at the second sub-pulse.

529 The 2D histograms in figure 2.5, reveal an important characteristics of our setup: in

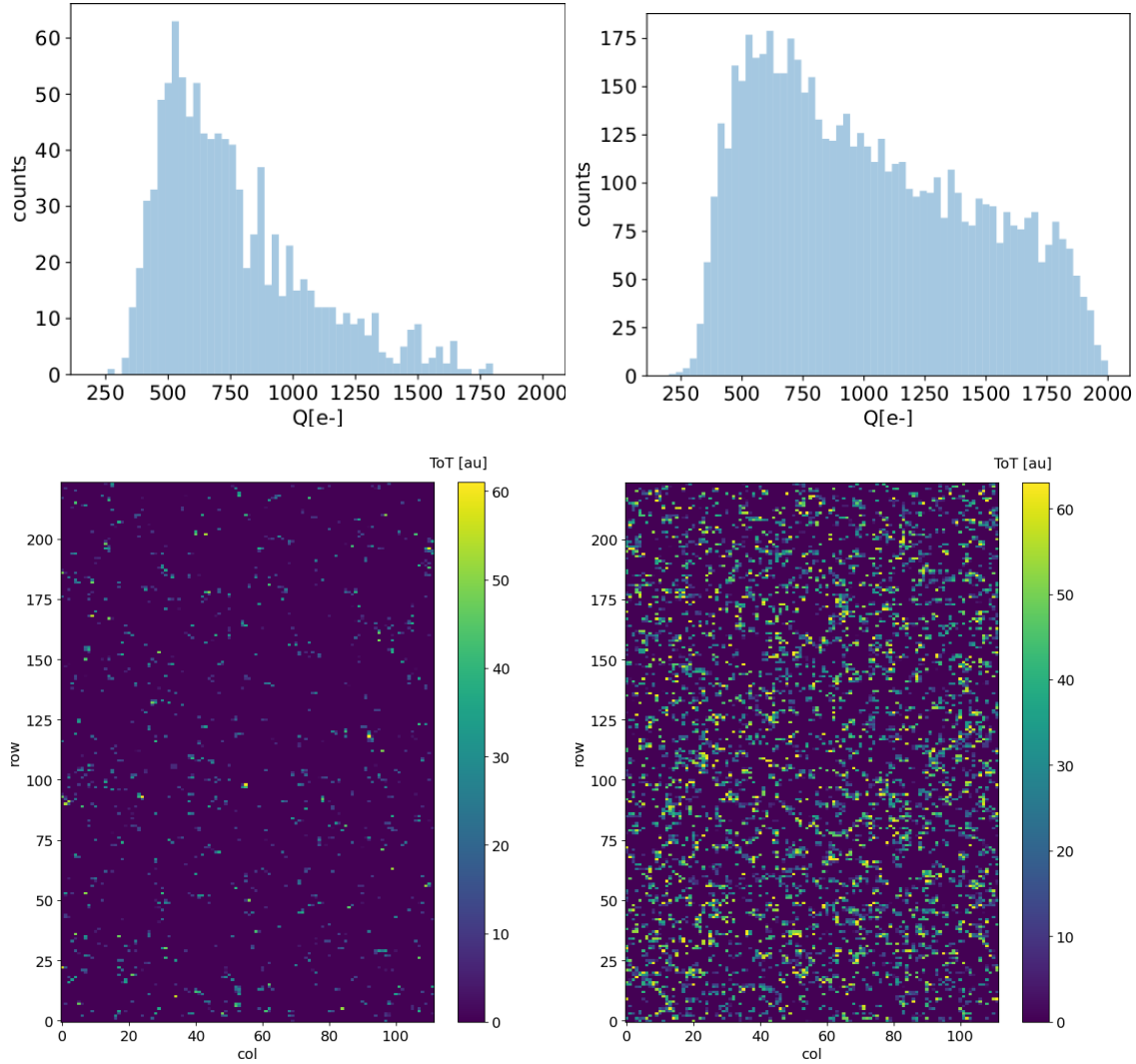


Figure 2.5: Acquisition with both the collimators: 5 pulses at $DDP=0.07\text{ Gy}$. (a) Spectrum of the charge released in the sensor: to apply the conversion I used the information found in the previous chapter. (b) 2D histogram of the ToT of the hits arrived in the sub-pulses.

fact, being uniform and not showing disomogenities, it follows that the collimators do not shield all the particles. We supposed that this was due to a Bremsstrahlung photon background higher than expected but a full verification of that and the analysis of the data is still going on. In figure 2.6, instead, the histograms with a higher DDP value is shown; in the example the matrix turns on completely, but again this happens in two different consecutive read chain.

When we have put aside the collimators, instead, the fluence increase a lot and the two-pulses substructure no more appears (fig. 2.7), but, because of the high attivity of the matrix, after each readout new hits with a fixed ToT were induced due to crosstalk. This problem had already been observed on other prototypes of TJ-Monopix1, and thanks to a simulation it has been observed that the main source of crosstalk is the voltage drop of the pre-amplifier ground as a result of the accumulated current that is drawn from the discriminator.

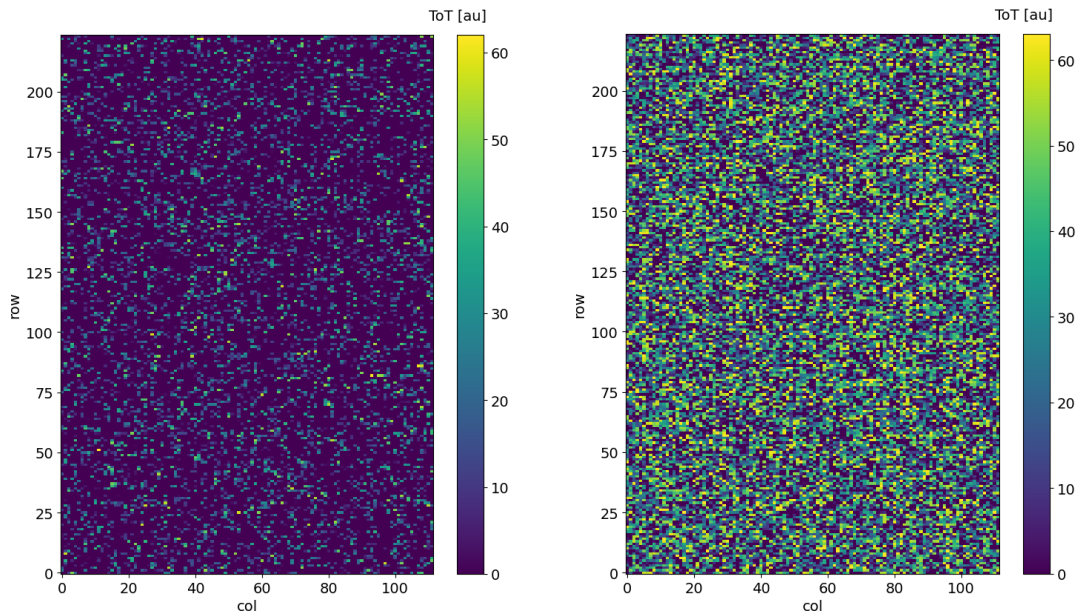


Figure 2.6: Acquisition with both the collimators: 5 pulses at $DDP=0.6\text{ Gy}$. 2D histogram of the ToT of the hits arrived in the sub-pulses. Compared with the previous maps, since the DDP is much higher, more pixels turn on.

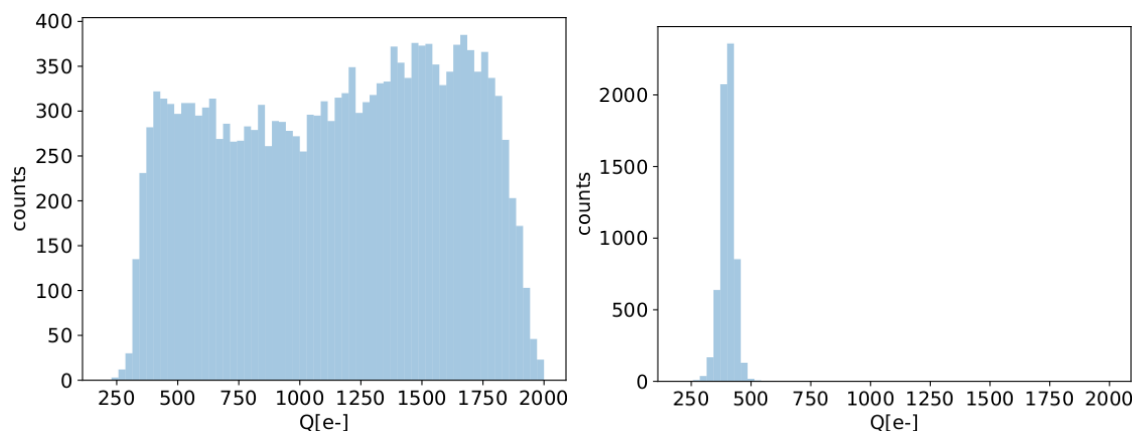


Figure 2.7: Acquisition without any collimator: 5 pulses at $DDP=0.04\text{ Gy}$.

543 Bibliography

- 544 [1] W. Snoeys et al. “A process modification for CMOS monolithic active pixel sensors
545 for enhanced depletion, timing performance and radiation tolerance”. In: (2017).
546 DOI: <https://doi.org/10.1016/j.nima.2017.07.046>.
- 547 [2] H. Kolanoski and N.Wermes. *Particle Detectors: Fundamentals and Applications*.
548 OXFORD University Press, 2020. ISBN: 9780198520115.
- 549 [3] E. Mandelli. “Digital Column Readout Architecture for 10.1109/NSSMIC.2009.5402399
550 the ATLAS Pixel 0.25 um Front End IC”. In: (2002).
- 551 [4] M. Garcia-Sciveres and N. Wermes. “A review of advances in pixel detectors for
552 experiments with high rate and radiation”. In: (2018). DOI: <https://doi.org/10.1088/1361-6633/aab064>.
- 554 [5] C. Marinas. “The Belle-II DEPFET pixel detector: A step forward in vertexing in the
555 superKEKB flavour factory”. In: (2011). DOI: [doi:10.1016/j.nima.2010.12.116](https://doi.org/10.1016/j.nima.2010.12.116).
- 556 [6] J. Baudot. “First Test Results Of MIMOSA-26, A Fast CMOS Sensor With Inte-
557 grated Zero Suppression And Digitized Output”. In: (2010). DOI: [doi:10.1109/NSSMIC.2009.5402399](https://doi.org/10.1109/NSSMIC.2009.5402399).
- 559 [7] A. Dorokhov. “High resistivity CMOS pixel sensors and their application to the
560 STAR PXL detector”. In: (2011). DOI: [doi:10.1016/j.nima.2010.12.112](https://doi.org/10.1016/j.nima.2010.12.112).
- 561 [8] Giacomo Contin. “The STAR MAPS-based PiXeL detector”. In: (2018). DOI: <https://doi.org/10.1016/j.nima.2018.03.003>.
- 563 [9] Nolan Esplen. “Physics and biology of ultrahigh dose-rate (FLASH) radiotherapy:
564 a topical review”. In: (2020). DOI: <https://doi.org/10.1088/1361-6560/abaa28>.
- 565 [10] Fabio Di Martino et al. “FLASH Radiotherapy With Electrons: Issues Related to
566 the Production, Monitoring, and Dosimetric Characterization of the Beam”. In:
567 *Frontiers in Physics* 8 (2020). ISSN: 2296-424X. DOI: [10.3389/fphy.2020.570697](https://doi.org/10.3389/fphy.2020.570697).
568 URL: <https://www.frontiersin.org/articles/10.3389/fphy.2020.570697>.
- 569 [11] M. Dyndal et al. “Mini-MALTA: Radiation hard pixel designs for small-electrode
570 monolithic CMOS sensors for the High Luminosity LHC”. In: (2019). DOI: <https://doi.org/10.1088/1748-0221/15/02/p02005>.
- 572 [12] M. Barbero. “Radiation hard DMAPS pixel sensors in 150 nm CMOS technology
573 for operation at LHC”. In: (2020). DOI: <https://doi.org/10.1088/1748-0221/15/05/p05013>.
- 575 [13] K. Moustakas et al. “CMOS Monolithic Pixel Sensors based on the Column-Drain
576 Architecture for the HL-LHC Upgrade”. In: (2018). DOI: <https://doi.org/10.1016/j.nima.2018.09.100>.

- 578 [14] I. Caicedo et al. “The Monopix chips: depleted monolithic active pixel sensors with
579 a column-drain read-out architecture for the ATLAS Inner Tracker upgrade”. In:
580 (2019). DOI: <https://doi.org/10.1088/1748-0221/14/06/C06006>.
- 581 [15] D. Kim et al. “Front end optimization for the monolithic active pixel sensor of the
582 ALICE Inner Tracking System upgrade”. In: *JINST* (2016). DOI: doi:10.1088/
583 1748-0221/11/02/C02042.
- 584 [16] L. Pancheri et al. “A 110 nm CMOS process for fully-depleted pixel sensors”. In:
585 (2019). DOI: <https://doi.org/10.1088/1748-0221/14/06/c06016>.
- 586 [17] L. Pancheri et al. “Fully Depleted MAPS in 110-nm CMOS Process With 100–300-
587 um Active Substrate”. In: (2020). DOI: 10.1109/TED.2020.2985639.